CESM/CAM5 Improvement and Application: Comparison and Evaluation of Updated CB05_GE and MOZART-4 Gas-Phase Mechanisms and Associated Impacts on Global Air Quality and Climate

Jian He[1], Yang Zhang[1*], Simone Tilmes[2], Louisa Emmons[2], Jean-Francois Lamarque[2], Tim Glotfelty[1], Alma Hodzic[2], and Francis Vitt[2]

[1] Department of Marine, Earth, and Atmospheric Science, North Carolina State University, Raleigh, NC

[2] National Center for Atmospheric Research, Boulder, CO

Abstract: Atmospheric chemistry plays a key role in determining the amounts and distributions of oxidants and gaseous precursors that control the formation of secondary gaseous and aerosol pollutants; all of those species can interact with the climate system. To understand the impacts of different gas-phase mechanisms on global air quality and climate predictions, in this work, a comprehensive comparative evaluation is performed using the Community Atmosphere Model (CAM) Version 5 with comprehensive tropospheric and stratospheric chemistry (CAM5-chem) within the Community Earth System Model (CESM) with two most commonly-used gas-phase chemical mechanisms: the 2005 Carbon Bond mechanism with Global Extension (CB05_GE) and the Model of OZone and Related chemical Tracers version 4 (MOZART-4) mechanism with additional updates (MOZART-4x). MOZART-4x and CB05_GE use different approaches to represent volatile organic compounds (VOCs) and different surrogates for secondary organic aerosol (SOA) precursors. MOZART-4x includes a more detailed representation of isoprene chemistry compared to CB05_GE. CB05_GE includes additional oxidation of

* Corresponding author: Yang Zhang, Email: yang_zhang@ncsu.edu, Phone: (919)-515-9688

SO_2 by O_3 over the surface of dust particles, which is not included in MOZART-4x. The results show that the two CAM5-chem simulations with CB05_GE and MOZART-4x predict similar chemical profiles for major gases (e.g., O_3, CO, and NO_x) compared to the aircraft measurements, with generally better agreement for NO_y profile by CB05_GE than MOZART-4x. The concentrations of SOA at four sites in continental U.S. (CONUS) and organic carbon (OC) over the IMPROVE sites are well predicted by MOZART-4x (with NMBs of -1.9% and 2.1%, respectively) but moderately underpredicted by CB05_GE (with NMBs of -23.1% and -20.7%, respectively). This is mainly due to the higher biogenic emissions and OH levels simulated with MOZART-4x than with CB05_GE. The concentrations of OC over Europe are largely underpredicted by both MOZART-4x and CB05_GE, with NMBs of -73.0% and -75.1%, respectively, indicating the uncertainties in the emissions of precursors and primary OC and relevant model treatments such as the oxidations of VOCs and SOA formation. Uncertainties in the emissions and convection scheme can contribute to the large bias in the model predictions (e.g., SO_2, CO, black carbon, and aerosol optical depth). The two simulations also have similar cloud/radiative predictions, with slightly better performance of domain average cloud condensation nuclei (CCN) at supersaturation of 0.5% by CB05_GE, but slightly better agreement with observed CCN (at supersaturation of 0.2%) profile over Beijing by MOZART-4x. The two gas-phase mechanisms result in a global average difference of 0.5 W m^{-2} in simulated shortwave cloud radiative forcing, with significant differences (e.g.,

up to 13.6 W m^{-2}) over subtropical regions.

Keywords: CB05_GE, MOZART-4, CAM5-chem, atmospheric gas-phase chemistry, secondary organic aerosol, model evaluation

1. Introduction

Atmospheric chemistry plays an important role in the perturbation of climate system by determining the amounts and distributions of important oxidants and gaseous precursors for secondary air pollutants such as ozone (O_3) and aerosols (IPCC, 2013). Aerosols can influence the Earth's radiative balance by directly scattering and absorbing radiation and indirectly affecting cloud properties through acting as cloud condensation nuclei (CCN) and ice nuclei (IPCC, 2013). The aerosol effects on radiation depend critically on their chemical composition and physical properties. Therefore, atmospheric chemistry is an important component for atmospheric and Earth system models. Different chemical mechanisms (e.g., different chemical reactions and kinetic parameters) can lead to differences in the predictions of gases, secondary aerosols, as well as climatic variables such as CCN, cloud droplet number concentration (CDNC), and radiative forcings (Luecken et al., 2008; Sarwar et al., 2008; Zhang et al., 2012a; Lamarque et al., 2013).

There are generally two types of species in the gas-phase mechanisms: inorganic and organic. Although most mechanisms include the same important inorganic species (e.g., O_3, carbon monoxide (CO), HO_x (odd hydrogen = hydroxyl radical () +

hydroperoxyl radical (HO_2)) and nitrogen oxides (NO_x)), the predicted amounts can vary greatly among different mechanisms (Knote et al., 2014a). Some mechanisms ignore reactions with very low reaction rates since they do not affect results significantly. Also, some reactions may use different rate coefficients with different dependence on atmospheric temperature and pressure due to the uncertainties in the laboratory measurements or the use of mechanisms that have not been updated in time. Unlike inorganic species, there are more significant differences in the representation of organic species. Light organic species with low molecular weight are often explicitly treated (e.g., methane, formaldehyde (HCHO)), whereas lumped or surrogate species are used to represent more complex mixtures of heavy organic compounds with high molecular weight (e.g., aromatics, organic nitrates). There are three most common representations of organic chemistry, including the lumped structure technique, the surrogate species approach, and the lumped species method (Zhang et al., 2004). For example, the Carbon Bond mechanism version IV (CB-IV, Gery et al., 1989), which uses the lumped structure approach for volatile organic compounds (VOCs), has been widely used in air quality modeling systems through urban to regional scales for many years. This mechanism has later been extensively updated in 2005 (CB05, Yarwood et al., 2005), and has been implemented into the Community Multiscale Air Quality model (CMAQ, Sarwar et al., 2008) and the Weather Research and Forecasting model with Chemistry (WRF-Chem, Wang et al., 2014). CB05 has been further expanded to include more than 120 reactions

that are important on global scale (CB05 with global extension (CB05_GE), Karamchandani et al., 2012) and implemented into global models, such as the Global-through-Urban WRF/Chem (GU-WRF/Chem, Zhang et al., 2012a) and the Community Atmosphere Model version 5 (CAM5), the atmospheric component of the Community Earth System Model (CESM/CAM5, He and Zhang, 2014). The Model of OZone and Related chemical Tracers version 4 (MOZART-4, Emmons et al., 2010) mechanism, which uses the lumped species approach for VOCs, has also been used in WRF-Chem (Knote et al., 2014b), and CAM with extensive tropospheric and stratospheric chemistry (CAM-chem) Versions 4 and 5 (Lamarque et al., 2012; Tilmes et al., 2015). Different gas-phase mechanisms have also been compared in several studies, however, most of which are conducted in box models or using regional models (Kim et al., 2009; Kim et al., 2011a, b; Yu et al., 2010). For example, using WRF-Chem, Zhang et al. (2012b) found that three different mechanisms (i.e., the Carbon Bond Mechanism-Z (CBM-Z), the 1999 Statewide Air Pollution Research Center Mechanism (SAPRC99), and the CB05) can predict different O_3 concentrations up to 5 ppb at surface in July, 2001. Yu et al. (2010) compared the O_3 predictions from three different mechanisms (i.e., CB4, CB05, and SAPRC99) using Eta-CMAQ and found that at the AIRNow surface sites, CB05 gives the best O_3 performance followed by CB4 and SAPRC-99 for observed $O_3 \geq 75$ ppb, whereas CB4 gives the best O_3 performance for observed $O_3 < 75$ ppb. Knote et al. (2014a) also compared seven chemical mechanisms using a box model and found that the differences

in daytime OH radical concentrations can be up to 40%.

Climate change can also strongly influence atmospheric chemistry and aerosols and therefore air quality. For example, photolysis and temperature-dependent reactions can be directly impacted by climate change (Jacob and Winner, 2009). Due to the nonlinear relationships between chemistry, aerosols, and climate, it is important to accurately represent their interactions in a three-dimensional global model. Several studies have demonstrated the capability of CAM-chem to represent tropospheric (Aghedo et al., 2011; Lamarque et al., 2010, 2011a, b; Tilmes et al., 2015) and stratospheric (Lamarque et al., 2008; Lamarque and Solomon, 2010) conditions. The chemical mechanism used in CAM-chem is based on MOZART-4, with detailed stratospheric chemistry of Kinnison et al. (2007). In this work, two most commonly used gas-phase mechanisms: the extended MOZART-4 (with updates as described by Knote et al. (2014b) and additional updates in this work) (referred to as MOZART-4x) and the CB05_GE chemical mechanisms are compared using the latest CESM/CAM5. The objectives are to examine the differences in the secondary organic aerosols (SOA) predictions resulted from the two gas-phase chemical mechanisms and study the sensitivity of air quality and climate predictions to different gas-phase chemical mechanisms.

2. Model Descriptions

The CESM/CAM5 used in this work is based on CAM version 5.3 of CESM version 1.2.2, coupled to comprehensive tropospheric and stratospheric chemistry (CAM5-chem, Tilmes et al., 2015) using the 7-mode Modal Aerosol Model (MAM7) (Liu et al., 2012). This version of CAM5-chem was further developed and improved at North Carolina State University (NCSU) in collaboration with NCAR, as described below. A more detailed description of this version of CESM CAM5-chem (referred to as CAM5-NCSU hereafter) used in this study can be found in He and Zhang (2014) and He et al. (2015).

2.1 Chemical Mechanisms

In this study, CB05_GE has been updated to include additional kinetic reactions describing interactions between functionalization and fragmentation processes during gas-phase oxidation of anthropogenic and biogenic VOCs by OH (Glotfelty et al., 2015). The products of those reactions are linked with the organic gas/particle partitioning for SOA formation. Heterogeneous reactions on tropospheric aerosols and stratospheric clouds are also added as same as those in MOZART-4x (Tilmes et al., 2015) with one additional pathway in CB05_GE to simulate sulfate formation through oxidation of sulfur dioxide (SO_2) by O_3 on the surface of dust particles.

MOZART-4x used in this work extends the MOZART chemical mechanism used in Lamarque et al. (2012) and Tilmes et al. (2015) to include several updates as described

144 in Knote et al. (2014b). These updates include (1) detailed treatments of monoterpenes
145 (α-pinene, β-pinene, and limonene) and 2-methyl-3-buten-2-ol (MBO); (2) detailed
146 treatments of aromatics (e.g., benzene, toluene, and xylenes); (3) additional glyoxal
147 ($C_2H_2O_2$) production from oxidized VOCs products; and (4) an updated isoprene (ISOP)
148 oxidation scheme. In this work, the oxidation of anthropogenic and biogenic VOCs and
149 subsequent aging processes are also included in MOZART-4x, and the products of those
150 reactions are linked with the organic gas/particle partitioning for SOA formation.
151 Table 1 shows the gas-phase organic precursors for SOA formation treated in
152 MOZART-4x and CB05_GE. For aromatic precursors of SOA, MOZART-4x includes
153 benzene, toluene (TOL), xylenes, and cresol. Although CB05_GE does not include
154 benzene, it includes polycyclic aromatic hydrocarbons (PAH) as a SOA precursor. For
155 alkane precursors of SOA, MOZART-4x includes BIGALK (lumped alkanes with carbon
156 (C) number > 3), whereas CB05_GE includes ALKH (long-chain alkanes, with C > 6).
157 For anthropogenic alkene precursors of SOA, MOZART-4x includes propene (C_3H_6) and
158 BIGENE (lumped alkenes with C >3), whereas CB05_GE includes terminal olefin (OLE)
159 and internal olefin (IOLE). The emissions for biogenic alkene precursors are from the
160 Model of Emissions of Gases and Aerosols from Nature version 2.1 (MEGAN2.1,
161 Guenther et al., 2012). Both MOZART-4x and CB05_GE include α-pinene (APIN), β-
162 pinene (BPIN), limonene, and ISOP as precursors for biogenic SOA. CB05_GE also
163 includes additional biogenic precursors such as speciated ocimene (OCI), humulene

(HUM) and terpinene (TER). However, in MOZART-4x, the species mapping for MEGAN emission calculation is slightly different. For example, α-pinene and other compounds (e.g., α-thujene, p-cymene, and o-cymene) are mapped into APIN, β-pinene and other compounds (e.g., sabinene and camphene) are mapped into BPIN, limonene and other compounds (e.g.; phellandrene and terpinene) are mapped into LIMON, myrcene and other compounds (e.g., ocimene) are mapped into MYRC, and beta-caryophyllene and other sesquiterpenes (e.g., humulene and α-bergamotene) are mapped into BCARY. Due to the different mapping for MEGAN species, biogenic emissions between MOZART-4x and CB05_GE are different, which can result in different biogenic SOA predictions. On the other hand, the rate coefficients for the oxidations of biogenic VOCs (e.g., APIN, BPIN, and limonene) are constant in CB05_GE, whereas they are temperature dependent in MOZART-4x, such a difference can result in different SOA predictions as well. In addition, there are uncertainties in the HO_x recycling associated with isoprene chemistry in CB05_GE (Karamchandani et al., 2012), whereas MOZART-4x used in this work includes OH recycling from improved isoprene chemistry. For example, in CB05_GE, ISOP is oxidized by OH to generate 91.2% molar yield of HO_2. In MOZART-4x, the isoprene peroxy radical from the oxidation ISOP by OH (i.e., ISOPO2) has different yields of HO_2 through reactions with nitrogen monoxide (NO), nitrate radical (NO_3), methylperoxy radical (CH_3O_2), and acetylperoxy radical (CH_3CO_3), and it can also consume HO_2 itself. These reactions have different reaction rate

coefficients. These differences can affect O_3, OH, and NO_x predictions, and thus the oxidation of VOCs.

2.2 Aerosol/Cloud Treatments

In CAM5-NCSU, the aerosol module is based on MAM7 of Liu et al. (2012), with improvements in terms of condensation, nucleation, aerosol thermodynamics, and aerosol activation (He and Zhang, 2014; Gantt et al., 2014). The major updates include: (1) the new particle formation treatments with a combination of the default nucleation parameterizations of Vehkamaki et al. (2002), Merikanto et al. (2007), and a newly added ion-mediated aerosol nucleation (Yu, 2010) above the planetary boundary layer (PBL), and a combination of the three and an additional parameterization of Wang and Penner (2009) in the PBL; (2) the inorganic aerosol thermodynamics based on ISORROPIA II of Fountoukis and Nenes (2007), which explicitly simulates the thermodynamics of sulfate (SO_4^{2-}), ammonium (NH_4^+), nitrate (NO_3^-), sodium (Na^+), and chloride (Cl^-) in the Aitken, accumulation, and fine sea-salt modes, as well as the impact of crustal species associated with the fine dust mode; (3) an advanced aerosol activation scheme based on Fountoukis and Nenes (2005) with additional updates based on Kumar et al. (2009) and Barahona et al. (2010), which accounts for adsorption activation from insoluble CCN and giant CCN equilibrium timescale on aerosol activation.

CAM5-NCSU also includes an advanced treatment for SOA formation based on a

volatility-basis-set (VBS) approach that has been coupled with CB05_GE by Glotfelty et al. (2015) and is also coupled with MOZART-4x in this work. This approach consists of two primary components: (1) volatile SOA (VSOA) formation from anthropogenic VOCs (AVOCs) and biogenic VOCs (BVOCs) and (2) the volatility and aging of primary organic aerosol (POA) and the repartitioning of the semi/intermediate volatility compounds (S/IVOC) into SOA. The VSOA treatment is based on the treatment of Tsimpidi et al. (2010). The products of VOC oxidation are mapped onto the volatility distribution using the aerosol mass yields listed in Tsimpidi et al. (2010) using the CB05_GE species that represent those precursor VOCs. An additional pathway for the formation of SOA from PAH is also added in CB05_GE. The SOA mass yields for PAHs are derived from the laboratory measurements of Chan et al. (2009) following the approach of Stainer et al. (2008), where the SOA mass yields for naphthalene, 1-methylnaphthalene, and 2-methylnaphthalene are averaged as surrogates for PAHs. The volatility of POA and the subsequent formation of SOA from POA vapors are based on the work of Robinson et al. (2007) and Shrivastava et al. (2008). POA emissions are distributed into nine logarithmically-spaced volatility bins with effective saturation (C*) values ranging from 10^{-2} to 10^{6} μg m^{-3}. An updated emission spectrum is used to distribute the POA emissions into the volatility bins as the emission spectrum used in Robinson et al. (2007) has been shown to be too volatile (Cappa and Jimenez, 2010; Hodzic et al., 2010; Jathar et al., 2011). This new emission spectrum maps the

anthropogenic POA emissions onto the volatility distribution based on thermodenuder measurements of gasoline exhaust and also contains separate emissions fractions for biomass burning aerosol which is less volatile than anthropogenic POA (May et al., 2013a, b). The emission spectrum of Robinson et al. (2007), also assumes that the emissions of SVOCs are fully captured by the original POA emissions and missing IVOCs are assumed to be equivalent to 1.5 times the POA emissions inventory with these additional emissions placed in the three highest volatility bins. However, because the estimations of the missing IVOC emissions are poorly constrained, the 1.5 times the POA mass for IVOCs is not included in this study.

In additional to the classic 1-D VBS treatment as described above, functionalization and fragmentation treatment described in Shrivastava et al. (2013) are included in this version of VBS for both VSOA and S/IVOCs (referred to as 1.5 D VBS). In this treatment, the VSOA and S/IVOCs in each volatility bin are split into three different species representing three generations of oxidation. During the first two generations of oxidation the mass of the VSOA and S/IVOCs grows by 15%, reflecting the addition of oxygen atoms. In this aging scheme not only do the masses of VSOA and S/IVOCs increase in generation when oxidized by OH (at a rate of 1.0×10^{-11} and 4.0×10^{-11} cm^3 $molecule^{-1}$ s^{-1}, respectively) but also their volatility decrease as they are moved into smaller volatility bins. Fragmentation occurs once the VSOA and S/IVOCs have aged to the third generation. This represents the breaking of carbon bonds, which can

increase volatility of the organic species thus reducing SOA formation. This is parameterized by allowing 17.25% of the organic mass to pass to the next lowest volatility bin but passing 75% of the VSOA and S/IVOC to the highest volatility bin in the VBS structure. The remaining mass is assumed to be lost to species of higher volatility than the VBS structure. There are several differences between the VBS used in this work and Shrivastava et al. (2015). For example, nine volatility bins are used in this work to represent the aging and gas-particle partitioning of POA, instead of five volatility bins used in Shrivastava et al. (2015). In addition, compared to the reaction (3) in Shrivastava et al. (2015), we do not have the third term, which denotes additional fragmentation where 10% of the mass results in low carbon number species with very high volatility that is eventually oxidized to CO/CO_2 and/or removed by dry deposition. In the model treatment used in this work, the remaining mass is assumed to be lost to species with a volatility higher than the volatility values in the VBS structure. A more detailed description of SOA formation from the VBS approach is summarized in Glotfelty et al. (2015).

3. Model Configurations and Evaluation Protocols

3.1 Model Setup and Inputs

The simulations are performed with specified dynamics configuration, of which winds and temperature are driven by the Goddard Earth Observing System Model,

264 Version 5 (GEOS-5) meteorology. The internally-derived meteorological fields are
265 nudged every time step (30 min) by 10% towards analysis fields from GEOS-5. The
266 nudged meteorological fields include surface pressure, meridional wind, zonal wind,
267 zonal surface stress, meridional surface stress, snow height, solar flux at surface, soil
268 moisture fraction, surface temperature, temperature, specific humidity, surface
269 geopotential, orography flag, surface water flux, and surface sensible flux. The
270 simulations are conducted for a 3-year period of 2008-2010 at a horizontal resolution of
271 $0.9^{o} \times 1.25^{o}$ and a vertical resolution of 56 layers for CAM5. The initial chemical
272 conditions are generated with same configurations with 1-year spinup.
273 The offline emissions used in this work are based on those used in Tilmes et al. (2015), of
274 which the anthropogenic and biofuel emissions are from the Monitoring Atmospheric
275 Composition and Climate/CityZen (MACCity) emission data set (Granier et al., 2011), and
276 biomass burning emissions are taken from the Atmospheric Chemistry and Climate Model
277 Intercomparison Project (ACCMIP) historical emissions dataset (Lamarque et al., 2010).
278 The ACCMIP emissions are extrapolated for 2008-2010 with the Representative
279 Concentration Pathway (RCP) 8.5 scenario and extended for VOCs and several other
280 species for MOZART-4x species. MOZART-4x species are then mapped into CB05_GE
281 species to generate emissions for CB05_GE species. Although both MOZART-4x and
282 CB05_GE simulates bromine chemistry, no bromine emissions are included. For
283 bromine/chlorine species (e.g., CF2CLBR, CF3BR, CFC11, CFC12, CH3BR, and

284 CH3CL), their surface concentrations are specified using the historical reconstruction from
285 Meinshausen et al. (2011). No bromine emissions were included.
286 The online emissions include biogenic VOCs from MEGAN2.1 (Guenther et al.,
287 2012), lightning NO_x (Price and Rind, 1992; Price et al., 1997), mineral dust (Zender et
288 al., 2003), and sea-salt (Martensson et al., 2003).
289
290 3.2 Available Measurements for Model Evaluation
291 A number of observational datasets from surface networks and satellites are used
292 for model evaluation. They are summarized along with the variables to be evaluated in
293 Table 2. The global surface network includes data sets from the National Oceanic and
294 Atmospheric Administration Climate Diagnostics Center (NOAA/CDC). The satellite
295 datasets include the Moderate Resolution Imaging Spectroradiometer (MODIS) for the
296 retrievals of cloud properties, the Clouds and Earth's Radiant Energy System (CERES)
297 Energy Balanced and Filled (EBAF) for the retrievals of radiation fluxes at surface and
298 top of atmosphere, the Aura Ozone Monitoring Instrument in combination with Aura
299 Microwave Limb Sounder (OMI/MLS) for the tropospheric ozone retrieval, the
300 Measurements Of Pollution In The Troposphere (MOPITT) for tropospheric carbon
301 monoxide (CO) retrieval, and the SCanning Imaging Absorption spectroMeter for
302 Atmospheric CHartographY (SCIAMACHY) for the retrievals of tropospheric nitrogen
303 dioxide (NO_2), HCHO, and $C_2H_2O_2$. Other satellite-based data include the MODIS-

304 derived CDNC and cloud liquid water path (LWP) by Bennartz (2007).

305 Regional observational networks include the Clean Air Status and Trends
306 Network (CASTNET), the Interagency Monitoring of Protected Visual Environments
307 (IMPROVE), the Speciation Trends Network (STN), and the Air Quality System (AQS)
308 over CONUS; the European Monitoring and Evaluation Program (EMEP), the Base de
309 Données sur la Qualité de l'Air (BDQA, France), and the European air quality database
310 (AirBase) over Europe; the Ministry of Environmental Protection of China (MEPC), the
311 National Institute for Environmental Studies of Japan (NIESJ), the Korean Ministry Of
312 Environment (KMOE), and Taiwan Air Quality Monitoring Network (TAQMN) over
313 East Asia. In addition to the data from the above networks, SOA measurements collected
314 by Lewandowski et al. (2013) at four field study sites including Cleveland and Medina,
315 OH (July-August, 2009), and Bakersfield and Pasadena, CA (May-June, 2010) are used
316 to evaluate SOA predictions.

317 Aircraft measurements include aircraft campaigns from Aerosol, Radiation, and
318 Cloud Processes affecting Arctic Climate (ARCPAC), Stratosphere-Troposphere
319 Analyses of Regional Transport in 2008 (START08), California Nexus 2010 (CalNex),
320 Arctic Research of the Composition of the Troposphere from Aircraft and Satellites
321 (ARCTAS), and CCN measurements in China (CCN_China). ARCPAC (Brock et al.,
322 2011) was conducted during March-April 2008 in the troposphere of the Alaskan Arctic,
323 including particle size distributions, composition, and optical properties. START08 (Pan

et al., 2010) was conducted during April-June 2008 to study the chemical and transport characteristics of the extratropical upper tropospheric and lower stratospheric region over central North America. CalNex (Ryerson et al., 2013) was conducted during May-July 2010 to provide improved scientific knowledge for emission control strategies to simultaneously address the interrelated issues of air quality and climate change. ARCTAS (Jacob et al., 2010) was conducted during April-June 2008 to investigate the chemistry of the Arctic's lower atmosphere. CCN_China (Zhang et al., 2011) was conducted over Beijing during July-September 2008, to investigate the impacts of aerosols on cloud formation.

3.3 Evaluation Protocol

The protocols for performance evaluation include spatial distributions and statistics, following the approach of Zhang et al. (2012b). The aircraft profile evaluation is based on the Atmospheric Model Working Group (AMWG) diagnostics package (Tilmes et al., 2015). Monthly-mean model results are compared for corresponding regions and seasons of the field campaign. The analysis of the performance statistics will focus on mean bias (MB), normalized mean bias (NMB), normalized mean error (NME), and root mean square error (RMSE) defined by Yu et al. (2006) and Zhang et al. (2006). The radiative/cloud variables are evaluated annually, including outgoing longwave radiation (OLR) from NOAA/CDC; downwelling shortwave radiation (FSDS),

downwelling longwave radiation (FLDS), shortwave cloud forcing (SWCF), and longwave cloud forcing (LWCF) from CERES-EBAF; cloud fraction (CF), aerosol optical depth (AOD), cloud optical thickness (COT), precipitating water vapor (PWV), and CCN from MODIS, as well as CDNC and LWP from Bennartz (2007). CDNC is calculated as an average value of layers between 850 and 960 hPa for comparison with the satellite-derived values. Chemical concentrations evaluated include CO, O_3, SO_2, ammonia (NH_3), NO_2, nitric acid (HNO_3), VOCs (i.e., formaldehyde, isoprene, and toluene), particulate matter (PM) with diameter less than and equal to 10 μm (PM_{10}) and 2.5 μm ($PM_{2.5}$), and $PM_{2.5}$ major components (e.g., SO_4^{2-}, NH_4^+, NO_3^-, black carbon (BC), organic carbon (OC), and total carbon (TC)) for CONUS and Europe. The chemical observations over East Asia are very limited, which only include surface observations of CO, SO_2, NO_2, and O_3 from Hong Kong, South Korea, and Japan, and PM_{10} over mainland China (derived from air pollution index), Hong Kong, South Korea, and Japan. Since $PM_{2.5}$ and PM_{10} are not explicit species simulated in MAM7, their concentrations are estimated based on size distributions of dry particles used in MAM7.. The properties of the particle size distribution for MAM7 are summarized in Table S1 in the supplementary material.

Column concentrations of tropospheric CO, NO_2, HCHO, $C_2H_2O_2$, and tropospheric O_3 residual (TOR) are evaluated for globe. The CO column evaluation follows the AMWG diagnostics approach, which applies $1^o \times 1^o$ monthly mean Level 3

MOPITT a priori and averaging kernels to monthly mean model results to account for the a priori dependence and vertical resolution of the MOPITT data. The measured NO_2 and HCHO columns are derived from the satellite retrievals from SCIAMCHY, which are monthly mean gridded data on a $0.25^o \times 0.25^o$ horizontal grid resolution for the period of 2008-2010. The measured glyoxal column is derived from the satellite retrievals from SCIAMCHY, which are monthly mean gridded data on a $0.125^o \times 0.125^o$ horizontal grid resolution for the period of 2008. The measured O_3 is derived from the combing retrievals from the Aura Ozone Monitoring Instrument and Microwave Limb Sounder observations, which are monthly mean gridded data on a $1.25^o \times 1.25^o$ horizontal grid resolution for the period of 2008-2010.

All surface observational data used for evaluating 2008-2010 simulations are available throughout 2008-2010 except for several variables with data during a limited time period of 2001-2010 including OC from EMEP, SOA from Lewandowski et al. (2013), and OA from Zhang et al. (2007) and Jimenez et al. (2009). For one grid cell containing multiple observational sites, all the observations within the grid cell are averaged and compared to the simulated results in that grid cell. While using grid averaged observations helps reduce, to some extent, the uncertainties in comparing grid averaged model output with pointwise observations, this approach cannot address the inherent uncertainties associated with the evaluation of the model results obtained at a coarse grid resolution.

4 Model Evaluations

4.1 Surface Evaluation

4.1.1 Inorganic Gases and Aerosols

Table 3 summarizes the performance statistics for major chemical species for CAM5-NCSU simulations with MOZART-4x and CB05_GE. Figure 1 shows the scatter plots between observations and model results. The statistical performance of MOZART-4x and CB05_GE are similar for most chemical species. As shown in Table 3, CO is underpredicted over East Asia by both MOZART-4x and CB05_GE, with NMBs of -65.6% and -65.7%, respectively. The underprediction of CO is mainly due to the underestimation of CO emissions from biomass burning (Tilmes et al., 2015). The underestimations in CO emissions lead to underpredictions of column CO concentrations, with NMBs of -25.8% and -24.4% for MOZART-4x and CB05_GE, respectively. Both MOZART-4x and CB05_GE largely overpredict the concentrations of SO_2 over CONUS (with NMBs of 580.2% and 561.6%, respectively), East Asia (with NMBs of 47.0% and 35.5% %, respectively), and Europe (with NMBs of 100.9% and 94.1%, respectively), likely due to the overestimation of SO_2 emissions, the uncertainties in the emission injection heights as well as the vertical mixing scheme used. For example, several modeling studies over East Asia reported the underestimates of emissions of SO_2 and NO_x are a main cause for poor model performance (e.g., Liu et al., 2010; Zhang et al.,

2015a, b). The overpredictions of surface SO_2 concentrations result in the overpredictions of the concentrations of SO_4^{2-} at the surface. The overpredictions of surface SO_4^{2-} concentrations can also be attributed to the uncertainties in the OH predictions. The air-mass weighted tropospheric mean OH concentrations predicted by MOZART-4x and CB05_GE are both 13.1×10^5 molec cm^{-3}, which is slightly higher than the present-day tropospheric mean OH level of 11.1 ± 1.6 molec cm^{-3} of Naik et al. (2013). The higher OH level can result in higher oxidation of SO_2 to produce more SO_4^{2-}. Surface NH_3 concentrations from MOZART-4x and CB05_GE are overpredicted over Europe (with NMBs of 112.4% and 104.3%, respectively), likely due to the overestimation of NH_3 emissions. The overpredictions of the NH_3 concentrations can potentially result in the overpredictions of the NH_4^+ concentrations at the surface. On the other hand, the overpredictions of the NH_4^+ concentrations at the surface are also related to the overpredictions of the concentrations of SO_4^{2-} at the surface. The concentrations of NO_2 from MOZART-4x and CB05_GE are largely underpredicted over CONUS (with NMBs of -51.4% and -52.2%, respectively), Europe (with NMBs of -61.4% and -62.1%, respectively), and East Asia (with NMBs of -74.1% and -74.8%, respectively), which is likely due to the uncertainties in estimating total NO_x emissions and emission injection heights as well. As shown in Figure 1, the concentrations of O_3 from MOZART-4x and CB05_GE are overpredicted over CONUS (with NMBs of 29.0% and 28.2% over the CASTNET sites, respectively), Europe (with NMBs of 19.3% and 22.2% over the EMEP

424 sites, respectively) and East Asia (with NMBs of 68.8% and 65.7% over the KMOE sites,
425 respectively). This is likely due to less O_3 titration resulted from the underpredictions of
426 NO_x, the dilution of NO_x emissions resulted from the use of a coarse grid resolution, as
427 well as possible underestimates in O_3 dry deposition. Martin et al. (2014) reported the
428 uncertainties in O_3 dry deposition associated with vegetation phenology in CAM-chem,
429 which led to positive biases of 16 ppb over eastern U.S. and 8 ppb over Europe,
430 respectively, for summertime surface O_3. The overpredictions of SO_4^{2-} result in the
431 underpredictions of NO_3^- and Cl^-, through thermodynamic equilibrium, and therefore
432 overpredictions of HNO_3 over CONUS. As more NH_4^+ are needed to neutralize SO_4^{2-},
433 less NH_4^+ are available to neutralize NO_3^- and Cl^-, driving total nitrate and total chlorine
434 to partition into the gas-phase to produce more HNO_3 and HCl. Yu et al. (2005) also
435 found that the model biases in total nitrate ($TNO_3 = HNO_3 + NO_3^-$) predictions can be
436 attributed to measurement errors in SO_4^{2-} and total ammonium ($TNH_4 = NH_3 + NH_4^+$) as
437 well as the inaccurate predictions in SO_4^{2-} and TNH_4. In addition, Reff et al. (2009)
438 suggested several sources for Cl^- (e.g., biomass burning and wildfires), which are not
439 included in this work. There are no anthropogenic Cl^- emissions included in this work
440 except from sea-salt emissions, which is calculated online in CESM/CAM5. Omission of
441 additional chlorine emissions may also partly explain the underpredictions of Cl^- over
442 CONUS. HNO_3 is underpredicted over Europe, which is mainly due to the
443 underpredictions of NO_x. The concentration of Cl^- is overpredicted over Europe, which is

likely due to the uncertainties for the gas/particle partitioning over coarse modes (He and Zhang, 2014). Unlike the performance of Cl^- over CONUS, which is only for fine Cl^- (in Aitken, accumulation, fine sea-salt, and fine dust modes), the performance of Cl^- over Europe is for fine and coarse Cl^- (in all seven modes). As the thermodynamic equilibrium is not treated for coarse particles (the irreversible condensation of HCl is assumed to occur on the surface of coarse particles), it is likely that the model overpredicts coarse Cl^-, but underpredicts fine Cl^- due to the missing sources. Both MOZART-4x and CB05_GE overpredict $PM_{2.5}$ over CONUS, however, they underpredict PM_{10} over the AQS sites, with NMBs of -38.6% and -38.9%, respectively. The underpredictions of PM_{10} are mainly due to the inaccurate predictions of coarse particles. Both MOZART-4x and CB05_GE underpredict $PM_{2.5}$ and PM_{10} over Airbase and BDQA sites, however, they overpredict PM_{10} by 3.14 $\mu g\ m^{-3}$ (or by 22.2%) and 3.43 $\mu g\ m^{-3}$ (or by 24.2%) over the EMEP sites, respectively, which is mainly due to the overpredictions of coarse particles (e.g., Cl^-) over these sites and uncertainties in the sea-salt and dust emissions. Both MOZART-4x and CB05_GE underpredict PM_{10} by 33.61 $\mu g\ m^{-3}$ (or by 33.4%) and 26.71 $\mu g\ m^{-3}$ (or by 26.6%) over the MEPC sites in mainland China, respectively, which is mainly due to the uncertainties in the emissions in primary gases (e.g., SO_2, NO_x, NH_3, and VOCs) and particulate species (e.g., SO_4^{2-}, BC, and POA). Granier et al. (2011) compared the regional emissions among different inventories and indicated large uncertainties in the emissions over China. For example, the differences of BC biomass

464 burning emissions over China among different inventories can be as large as a factor of
465 2.1, and the differences of SO_2 anthropogenic emissions can be as large as a factor of 1.8.
466 **4.1.2 VOCs and Organic Aerosols**
467 VOCs species such as HCHO, ISOP, and TOL are underpredicted over CONUS,
468 likely due to the uncertainties in the biogenic emissions from MEGAN2.1, anthropogenic
469 emissions (e.g., HCHO and TOL) and the chemical reactions as well as a coarse
470 horizontal resolution used in this work. Both MOZART-4x and CB05_GE underpredict
471 BC with NMBs of -29.3% and -29.3%, respectively. The underpredictions of BC are
472 likely due to the underestimations of BC emissions, as well as uncertainties in the
473 transport and wet removal by convection (Ma et al., 2013; Wang et al., 2013; Tilmes et
474 al., 2015).
475 OC is slightly overpredicted with an NMB of 2.1% by MOZART-4x over
476 CONUS, whereas it is moderately underpredicted with an NMB of -20.7% by CB05_GE.
477 OC is evaluated against observations at the IMPROVE sites, and SOA dominates OC at
478 these sites for both simulations with MOZART4-x and CB05_GE, with SOA/OC ratios
479 of 83.0% and 59.6%, respectively. Although no SOA measurements are available from
480 IMPROVE for evaluation, the differences in OC predictions can be attributed to the
481 differences in SOA predictions because of dominances of SOA in total OC. Compared to
482 the SOA observations at the four sites in the U.S. from Lewandowski et al. (2013),
483 MOZART-4x underpredicts SOA by 0.03 μg m^{-3} (or by 1.9%), whereas CB05_GE

484 underpredicts SOA by 0.4 μg m^{-3} (or by 23.1%). Note that the SOA statistics are
485 calculated using only four pairs of seasonal mean values at four sites in the U.S. where
486 the observed SOA data are available during 2008-2010; they therefore may not be
487 representative because of limited data used for calculation. Figure 2 compares simulated
488 and observed SOA concentrations at the four sites. MOZART-4x predicts higher SOA
489 than CB05_GE at all four sites, which reduces underpredictions at Cleveland and
490 Medina, OH but increases overpredictions at Bakersfield and Pasadena, CA. This
491 indicates a better capability of MOZART-4x to simulate SOA at sites with relatively high
492 SOA concentrations (≥ 1 μg m^{-3}) compared to CB05_GE despite its tendency of
493 overpredictions at sites with lower SOA levels. The higher SOA concentrations predicted
494 by MOZART-4x can be attributed to the higher OH levels and higher biogenic emissions
495 in MOZART-4x. However, the concentration of OC is largely underpredicted by both
496 MOZART-4x and CB05_GE over Europe, with NMBs of -74.2% and -75.1%,
497 respectively, indicating the uncertainties in the emissions of SOA precursors and SOA
498 formation treatment. For example, the aqueous-phase oxidation of VOCs in clouds is not
499 taken into account in this work, which, however, can contribute several percentages of
500 SOA in some areas and seasons over Europe (Couvidat et al., 2013). The hydrocarbon-
501 like organic aerosol (HOA) predicted by MOZART-4x and CB05_GE correlated well
502 with the observations at 33 sites in the Northern Hemisphere (e.g., with correlation
503 coefficients of 0.93 for both simulations) but the amount is largely underpredicted by

both MOZART-4x and CB05_GE, with NMBs of -77.2% and -76.7%, respectively, indicating that the POA may be too volatile with the implementation currently in the model. Oxygenated organic aerosol (OOA), which is roughly equivalent to the sum of SOA and SVOA, is also largely underpredicted at the 33 sites by both MOZART-4x and CB05_GE, with NMBs of -56.5% and -62.3%, respectively. This is mainly due to the uncertainties in the oxidation rate and fragmentation rates as well as SOA formation treatment. The underpredictions of HOA and OOA result in an underprediction of total organic aerosol (TOA) by both MOZART-4x and CB05_GE, with NMBs of -67.8% and -71.2%, respectively.

4.2 Chemical Column Evaluation

Figure 3 shows the zonal mean of column concentrations of CO, HCHO, glyoxal, NO_2, and TOR for June, July, and August during 2008-2010. In general, MOZART-4x and CB05_GE predict similar zonal mean profiles of these species. Both MOZART-4x and CB05_GE underpredict column CO, due to a significant underestimation of CO emissions (Tilmes et al., 2015) and uncertainties in OH predictions. During summer, column HCHO is overpredicted over middle latitudes (30-60^o N) in the Northern Hemisphere and tropical regions (0-10^o S) in the Southern Hemisphere, while it is largely underpredicted over the rest of regions. The underprediction of column HCHO is likely due to the uncertainties in the emissions of HCHO and its precursors as well as pathways for secondary HCHO formation. Both MOZART-4x and CB05_GE underpredict column

524 glyoxal, with more underpredictions in CB05_GE. The underpredictions of glyoxal are
525 mainly due to the uncertainties in the glyoxal chemical production and removal (Knote et
526 al., 2014b). Several studies indicate that aromatics, isoprene, and ethyne are the major
527 contributors to glyoxal formation (Washenfelder et al., 2011; Knote et al., 2014b). In
528 MOZART-4x, glyoxal can be produced from photolysis of the oxidation products of
529 toluene, and oxidation products of aromatics (e.g., benzene, toluene, and xylenes),
530 isoprene, and ethyne. CB05_GE does not include pathways for glyoxal production
531 through photolysis, but includes glyoxal production from oxidation of alkenes (e.g., OLE,
532 IOLE, ethene, and ISOP) and aromatics (e.g., toluene and xylenes). Uncertainties in the
533 emissions of these precursors and the production pathways can propagate into the
534 predicted glyoxal concentrations. MOZART-4x includes additional pathways for glyoxal
535 production through photolysis and improved treatments for glyoxal production from
536 additional oxidized VOCs (e.g., benzene) products (Knote et al., 2014b), which can result
537 in higher glyoxal than in CB05_GE. The major chemical loss of glyoxal includes
538 photochemical loss and oxidation by OH. The uncertainties in OH levels can propagate
539 into glyoxal predictions as well. In addition, CB05_GE includes an additional pathway
540 for glyoxal loss through its uptake by aerosols, which is not included in MOZART-4x.
541 This can explain in part the lower glyoxal concentrations predicted by CB05_GE than by
542 MOZART-4x. An advanced treatment for glyoxal formation should be therefore
543 developed in the future. Both MOZART-4x and CB05_GE overpredict column NO_2,

likely due to the uncertainties in the NO_2 aircraft emissions and overpredictions of lightning NO_x, as well as the satellite retrievals. The lightning NO_x emissions are calculated online (i.e., 6.2 and 6.4 TgN yr^{-1} in CB05_GE and MOZART-4x, respectively), which is about 1.2-2.2 TgN yr^{-1} higher than that in Lamarque et al. (2012) and Tilmes et al. (2015). Tilmes et al. (2015) have shown that increased lightning NO_x emissions in CAM-chem can lead to an increase in OH levels and therefore a decrease in the lifetime of methane and an underestimation of CO in the model. As discussed in Yarwood et al. (2012), the errors in satellite NO_2 retrievals are dominated by atmospheric mass factor, which has a large uncertainty due to errors in the specification of clouds, surface albedo, a priori NO_2 profile shape, and aerosols. Boersma et al. (2004) also reported that the error in the tropospheric NO_2 retrievals is 35-60%, especially over polluted areas. These can partly explain the overpredictions of column NO_2. The higher zonal-mean concentrations of NO_2 in CB05_GE than those in MOZART-4x are likely due to additional NO_2 production from the reactions of VOCs with NO_3 radical in CB05_GE (e.g., reactions of NO_3 with OLE, IOLE, and ethene). The zonal-mean distribution of summer TOR from CB05_GE is similar to that from MOZART-4x. TOR is overpredicted over 40^o S-50^o N, and underpredicted over 40^o S-60^o S. The higher TOR from CB05_GE is mainly due to higher O_3 production from higher NO_2 and lower O_3 loss from lower OH in CB05_GE than in MOZART-4x.

4.3 Vertical Profile Evaluation

564 Figure 4 compares the vertical profile of major gases against the aircraft
565 observations (i.e., ARCPAC, ARCTAS, START08, and CalNex). Compared with aircraft
566 measurements, MOZART-4x and CB05_GE predict similar O_3 and CO profiles, whereas
567 there are large differences in NO_x (above 9 km) and NO_y profiles (below 12 km). O_3
568 profiles from MOZART-4x and CB05_GE overall agree well with aircraft measurements,
569 although O_3 is slightly overpredicted near the surface. As discussed previously, the
570 significant underpredictions of CO profiles in both MOZART-4x and CB05_GE are
571 mainly due to the underestimations of CO biomass burning emissions and uncertainties in
572 OH predictions. Both MOZART-4x and CB05_GE underpredict the vertical
573 concentrations of NO_x at higher altitudes (e.g., above 9 km in ARCTAS and STRAT08),
574 with a slightly better agreement in CB05_GE than in MOZART-4x. The concentrations of
575 NO_x near the surface are slightly overpredicted by both simulations. The underpredictions
576 of the concentrations of NO_x at higher altitudes are likely due in part to the uncertainties
577 in the NO_x emissions, the chemical reactions of nitrogen cycles (e.g., heterogeneous
578 reactions of NO_2, NO_3, and N_2O_5 over the surface of aerosol particles), the convection
579 scheme, as well as the aircraft campaign data. Some field campaigns (e.g., ARCPAC)
580 focus on the polluted regions with a significant contribution from biomass burning and
581 local sources (Tilmes et al., 2015). The underestimations of emissions from these sources
582 and uncertainties in the vertical mixing scheme can result in the underpredictions of their
583 profiles. NO_y includes all the reactive nitrogen species. The simulated NO_y profiles from

584 CB05_GE agree better with those observed during APCPAC, ARCTAS, and CalNex than
585 those from MOZART-4x, whereas MOZART-4x predicts slightly better NO_y profile
586 against START08 in the lower troposphere than CB05_GE. OH concentrations are
587 underpredicted by both MOZART-4x and CB05_GE against ARCTAS observations,
588 whereas H_2O_2 mixing ratios are well predicted above 4 km but underpredicted below 4
589 km. Compared to CB05_GE, MOZART-4x predicts slightly higher H_2O_2 within 4-km
590 above the surface. However, the performance here only represents the local conditions,
591 instead of global conditions. Figure 5 compares the vertical profile of simulated CCN
592 against the aircraft observations from CCN_China. Both MOZART-4x and CB05_GE
593 slightly overpredict CCN (at supersaturation of 0.2%) profile over Beijing area, with less
594 overpredictions in MOZART-4x.

595 **4.4 Cloud/Radiative Evaluation**

596 Table 4 shows the statistical performance for major cloud/radiative variables for
597 MOZART-4x and CB05_GE simulations. Radiative variables such as OLR, FSDS, and
598 FLDS show excellent agreement with observations, with NMBs within ±8% for both
599 simulations. However, SWCF is overpredicted by both MOZART-4x and CB05_GE, with
600 NMBs of 26.4% and 27.7%, respectively, and LWCF is underpredicted by both
601 MOZART-4x and CB05_GE, with NMBs of -21.6% and -16.7%, respectively. All
602 predicted radiative variables show high correlation with observations, with correlation
603 coefficients of 0.9 to 0.99. CF is well predicted by MOZART-4x, with an NMB of 6.3%,

604 whereas CCN5, CDNC, COT, and LWP are moderately overpredicted or underpredicted,
605 with NMBs of -32.1%, 19.7%,-26.0%, and 2.8%, respectively. The performance of cloud
606 variables is similar in CB05_GE, with NMBs of 6.0%, -29.0%, 20.8%, -26.0%, and 1.7%
607 for CF, CCN5, CDNC, COT, and LWP, respectively. AOD is also underpredicted by both
608 MOZART-4x and CB05_GE, with NMBs of -23.9% and -24.6%, respectively.

609 Figure 6 shows the Taylor diagram (Taylor, 2001) comparing the model
610 performance of MOZART-4x with that of the CB05_GE for cloud and radiative
611 predictions. The similarity between the two patterns is quantified in terms of their
612 correlations (i.e., angle), their standard deviations (i.e., y axis), and the ratio of their
613 variances (i.e., x axis). In general, the performance of major cloud/radiative variables
614 between MOZART-4x and CB05_GE are similar. The major differences in the
615 performance of cloud/radiative variables between MOZART-4x and CB05_GE are the
616 variances of CCN5, CDNC, and SWCF, which is mainly due to the predicted aerosol
617 distributions. The larger deviation of COT and LWP from observations (i.e., the two
618 points located outside the diagram in Figure 6) suggests the uncertainties both in the
619 model treatments for cloud dynamics and thermodynamics as well as in the satellite
620 retrievals.

621 Due to the underpredictions of cloud variables (e.g., COT and CCN5), OLR is
622 slightly overpredicted by 7.8 W m^{-2} (or by 3.6%), and LWCF is underpredicted by 4.8 W
623 m^{-2} (or by 21.6%) in MOZART-4x. Similarly, OLR is slightly overpredicted by 6.7 W m^{-2}

624 (or by 3.1%) and LWCF is underpredicted by 3.7 W m^{-2} (or by 16.7%) in CB05_GE.
625 Figure 7 shows the comparisons of satellite observations with model predictions for
626 AOD, CCN5, CDNC, COT, and SWCF averaged during 2008-2010. The
627 underpredictions of AOD over oceanic areas can be attributed to the uncertainties in the
628 sea-salt emissions and inaccurate predictions of other PM components (e.g., marine
629 organic aerosols) over the ocean and overestimation of oceanic AOD in the MODIS
630 collection 5.1 (Levy et al., 2013). The underprediction of AOD over land (e.g., tropical
631 islands) is mainly due to the significant underestimation of biomass burning emissions in
632 the model (Tilmes et al., 2015). AOD is higher in MOZART-4x over most land areas
633 (except East Asia and Europe) than in CB05_GE. The higher AOD in MOZART-4x is
634 mainly due to higher SOA (e.g., over most land areas) and higher NO_3^- (e.g., over
635 CONUS) in MOZART-4x. The lower AOD over East Asia and Europe in MOZART-4x is
636 mainly due to the lower SO_4^{2-} as there is an additional pathway of SO_2 (oxidized by O_3)
637 included in CB05_GE but it is not included in MOZART-4x and lower NH_4^+ to neutralize
638 lower SO_4^{2-} through thermodynamic equilibrium. This additional pathway also results in
639 higher H_2SO_4 predictions in CB05_GE and higher aerosol number concentration through
640 homogeneous nucleation. Therefore, CCN5 is higher in CB05_GE than in MOZART-4x
641 (see Figure 7). CDNC is moderately overpredicted for both cases. Cloud droplet
642 formation is sensitive to both particle number concentrations and updraft velocity
643 (Reutter et al., 2009). The overprediction of CDNC is due partly to high activation

644 fractions (e.g., inclusion of adsorption activation from insoluble CCN and effective
645 uptake coefficient of 0.06 used in this work) (Gantt et al., 2014) as well as the
646 uncertainties in the model treatments for cloud microphysics (e.g., resolved clouds and
647 subgrid-scale cumulus clouds) and satellite retrievals (e.g., error propagation of the input
648 variables to derive CDNC) (Bennartz, 2007). COT is largely overpredicted over
649 Southeast Asia and South America and underpredicted over polar regions for both
650 simulations. Overpredictions in CDNC and COT can increase cloud albedo and therefore,
651 increase SWCF over the low and middle latitudes. The large underpredictions of COT
652 over polar regions can be attributed to the uncertainties in plane-parallel visible-near-
653 infrared retrievals with low solar zenith angle (Seethala and Horváth, 2010) and the
654 influence of radiatively active snow on overlying cloud fraction (Kay et al., 2012). Due to
655 the different gas-phase mechanisms, the predicted SWCF (Figure 7) and LWCF (Figure
656 not shown) are different, with a global average difference of 0.5 W m^{-2} and 1.1 W m^{-2},
657 respectively. However, the absolute differences in simulated SWCF can be as large as
658 13.6 W m^{-2} as shown in Figure 7. The large differences of SWCF and LWCF between
659 MOZART-4x and CB05_GE are mainly over subtropical regions (e.g., 20 ^{o}S - 20 ^{o}N),
660 which is mainly due to lower COT in MOZART-4x than in CB05_GE.
661

662 **5. Model-to-Model Comparisons**

663 **5.1 Column Comparisons**

664 **5.1.1 Column Gases**

665 Figures 8a and b compare the column mass abundance of major gaseous and
666 aerosol species simulated by MOZART-4x and CB05_GE. As shown in Figure 8a,
667 column CO predicted by MOZART-4x is about 2.4×10^{20} m^{-2} (or by 2.3%) lower than that
668 by CB05_GE in the global mean. The different column CO concentrations are due to
669 different pathways for chemical production and loss of CO between MOZART-4x and
670 CB05_GE, and different OH levels in MOZART-4x and CB05_GE. The chemical
671 production of CO is mainly from photolysis and oxidation of VOCs species, and the
672 chemical loss of CO is mainly from the oxidation by OH. Different concentrations of
673 VOCs species can result in different chemical production of CO. Meanwhile, the only
674 chemical loss of CO in CB05_GE is the oxidation of CO by OH, which produces HO_2
675 and CO_2. Higher OH levels in MOZART-4x can result in more CO loss. MOZART-4x
676 includes an additional loss pathway of CO oxidized by OH to produce CO_2 and H. As a
677 result, the combined rate constant for both pathways of CO oxidation by OH in
678 MOZART-4x is about 4% higher than in CB05_GE. All these differences result in 2301
679 and 2265 Tg yr^{-1} chemical loss of CO in MOZART-4x and CB05_GE, respectively.

680 The global mean differences in the simulated column concentrations of SO_2 and
681 NH_3 between MOZART-4x and CB05_GE are 2.0×10^{18} m^{-2} (or by 12.5%) and 1.9×10^{17}
682 m^{-2} (or by 3.1%), respectively. The lower column abundance of SO_2 in CB05_GE is
683 mainly due the additional pathway for SO_2 loss through oxidation by O_3 over the surface

684 of dust particles, which is not included in MOZART-4x. This pathway can produce more
685 SO_4^{2-} and therefore, more NH_3 is partitioned into the particulate phase to form NH_4^+
686 which can neutralize additional SO_4^{2-}, resulting in lower column abundance of NH_3 in
687 CB05_GE. Both column concentrations of NO_x and NO_y from MOZART-4x are about
688 9.4×10^{17} m^{-2} (or by 9.5%) and 3.6×10^{19} m^{-2} (or by 46.3%) lower than that from
689 CB05_GE. The higher NO_x in CB05_GE is mainly due to the lower OH available for the
690 chemical loss through the reaction of NO_2 with OH. NO_y in MOZART-4x includes NO_x,
691 nitrate radical (NO_3), nitrogen pentoxide (N_2O_5), HNO_3, peroxynitric acid (HO_2NO_2),
692 chlorine nitrate ($ClONO_2$), bromine nitrate ($BrONO_2$), peroxyacetyl nitrate (PAN),
693 organic nitrate (ONIT), methacryloyl peroxynitrate (MPAN), peroxy radical from the
694 reaction of NO_3 with ISOP (ISOPNO3), and lumped isoprene nitrate (ONITR), whereas
695 NO_y in CB05_GE includes NO_x, NO_3, N_2O_5, HNO_3, HO_2NO_2, $ClONO_2$, $BrONO_2$, nitrous
696 acid (HONO), PAN, higher peroxyacyl nitrates (PANX), and organic nitrate (NTR). The
697 reactions for reactive nitrogen species are different in MOZART-4x and CB05_GE,
698 resulting in different NO_y predictions. Figure S1 in the supplementary material shows the
699 dominant species in NO_y predicted by the simulations using both MOZART-4x and
700 CB05_GE. As shown in Figure S1, NO_x, HNO_3, and TPAN (PAN+MPAN for MOZART-
701 4x and PAN+PANX for CB05_GE) are the major components for NO_y concentrations,
702 with the ratios of 90.5% and 91.7%, respectively, for the sum of the mixing ratios of top
703 three species to that of NO_y. NO_x dominates over East Asia, eastern U.S., and western

704 Europe, whereas TPAN dominates over most oceanic area. Figure S2 in the
705 supplementary material shows the absolute and relative differences for major NO_y species
706 between MOZART-4x and CB05_GE. As shown in Figure S2, MOZART-4x predicts
707 lower column TPAN by 2.9×10^{19} molecules m^{-2} (or by 63.4%), which dominates the
708 differences in NO_y predictions between the two simulations. The differences in TPAN
709 predictions can be attributed to the differences in the kinetic reactions. Table S2 in the
710 supplementary material lists the reactions involving TPAN. As shown in Table S2,
711 besides the differences in the reaction rate calculation, MOZART-4x includes one
712 additional reaction, i.e., PAN destruction by OH, which is not included in CB05_GE. In
713 addition, simulated OH levels are higher in MOZART-4x than those in CB05_GE, which
714 could result in more TPAN loss through oxidation by OH. These differences can explain
715 the lower TPAN mixing ratios in MOZART-4x than those in CB05_GE and thus lower
716 column NO_y mass abundances in MOZART-4x than those in CB05_GE. Table S3 in the
717 supplementary material lists the NO_y species used in the calculation for Figure 4 and
718 other NO_y related comparisons. Figure S3 in the supplementary material shows the
719 absolute differences in NO_y (with and without inclusion of aerosol nitrate) between
720 MOZART-4x and CB05_GE. If aerosol nitrate is accounted for in the NO_y definition, the
721 differences in NO_y between the two mechanisms decrease over East Asia, eastern U.S.,
722 Europe, and middle Africa as aerosol nitrate is higher in MOZART-4x over these regions
723 (see Figure 6b). For the rest of areas, the differences in NO_y between the two mechanisms

724 increase if aerosol nitrate is accounted for in the NO_y definition.The tropospheric column
725 O_3 from MOZART-4x is about 1.5 DU (or by 4.7%) lower than that from CB05_GE.
726 Table 5 shows the tropospheric O_3 budget from MOZART-4x and CB05_GE. The
727 burdens of tropospheric O_3 from MOZART-4x and CB05_GE are 325 Tg and 333 Tg,
728 respectively, which is comparable to the previous studies using CAM (Lamarque et al.,
729 2012; Young et al., 2013). The O_3 burden from MOZART-4x in this work is about 12 Tg
730 (or 3.8%) higher than that in Tilmes et al. (2015), which is mainly due to the additional
731 kinetic reactions included in this version of MOZART-4x. The dry deposition flux of O_3
732 from MOZART-4x is 679 Tg yr^{-1}, which is about 3.7% lower than that from CB05_GE
733 (i.e., 705 Tg yr^{-1}). The lower O_3 dry deposition flux is mainly due to the lower O_3
734 concentration simulated by MOZART-4x. The O_3 chemical production and loss from
735 CB05_GE and MOZART-4x are roughly within the range of Young et al. (2013). The O_3
736 chemical production from MOZART-4x is comparable to that of Lamarque et al. (2012),
737 but the O_3 chemical production from CB05_GE is about 12.8% higher than Lamarque et
738 al. (2012). In this table, chemical production is calculated mainly from reactions of NO
739 with peroxy radicals and chemical loss is calculated mainly from the oxygen radical in
740 the reaction of excited oxygen atom (O^1D) with water vapor (H_2O) and from the reactions
741 of O_3 with the HO_2, OH, and alkenes. Different peroxy radicals and alkenes treated and
742 different reaction rates used in the two mechanisms can contribute to the different
743 chemical production and chemical loss of O_3. The O_3 lifetime is calculated based on the

744 ratio of O_3 burden to the total O_3 loss (dry deposition + chemical loss). The O_3 lifetime
745 from CB05_GE is comparable to those reported by Young et al. (2013), and the O_3
746 lifetime from MOZART-4x is comparable to those reported by Lamarque et al. (2012)
747 and Tilmes et al. (2015).

748 Column concentrations of OH, HCHO, and ISOP from MOZART-4x are higher
749 than CB05_GE, with global mean values of 9.7×10^{13} m^{-2} (or by 0.8%), 3.5×10^{17} m^{-2} (or
750 by 1.3%), and 1.1×10^{18} m^{-2} (or by 25.6%), respectively. The higher column
751 concentrations of OH and HCHO are likely due to the photolysis of more peroxide
752 species, better HO_x recycling, and higher precursors for secondary HCHO (e.g., ISOP) in
753 MOZART-4x. MOZART-4x includes detailed organic peroxide species, whereas in
754 CB05_GE, all the organic peroxide species are lumped into one species (i.e., ROOH).
755 The uncertainties in HO_x recycling in CB05_GE can also result in uncertainties in OH
756 predictions. The higher ISOP is mainly due to higher biogenic emissions and less
757 chemical loss in MOZART-4x than that in CB05_GE. In MOZART-4x, the chemical loss
758 of ISOP is mainly from the oxidation of ISOP by OH, O_3, and NO_3. However, in
759 CB05_GE, the chemical loss of ISOP includes not only the oxidation of ISOP by OH, O_3,
760 and NO_3, but also the consumption of ISOP by atomic oxygen (i.e., O), NO_2, and Cl.

761 **5.1.2 Column Aerosols**

762 As shown in Figure 8b, the differences in the domain average column mass
763 abundances of most aerosol species (e.g., NH_4^+, BC, Cl^-, and POA) between MOZART-

764 4x and CB05_GE are within ± 0.02 mg m^{-2}. The differences in the column SO_4^{2-} vary
765 from -25.2 to 0.4 mg m^{-2}, with the global mean of -0.2 mg m^{-2}. The simulated column
766 concentrations of SO_4^{2-} from MOZART-4x are much lower than those from CB05_GE
767 over East Asia, west Europe, and Middle Africa. SO_2 can be oxidized by O_3 to form SO_4^{2-}
768 on the surface of dust particles in CB05_GE, which explains additional formation of
769 SO_4^{2-} by CB05_GE over these regions. The differences of the spatial distributions and
770 magnitudes in the column concentrations of NH_4^+ are similar to those of SO_4^{2-} over land
771 areas, which is associated with thermodynamic equilibrium. The column concentrations
772 of NO_3^- simulated by MOZART-4x are higher over East Asia, India, and Europe than
773 those by CB05_GE, which is mainly due to its competition with SO_4^{2-} in forming
774 ammonium salts in the particulate phase in those regions where the column NH_3
775 concentrations are high (Figure 8a). Dust emissions are very sensitive to the wind speed.
776 Slightly changes in wind speeds can result in significant change in dust emissions, thus,
777 dust concentrations.

778 The column concentrations of SOA predicted by MOZART-4x are about 0.18 mg
779 m^{-2} (or by 8.4%) higher than those predicted by CB05_GE. The higher SOA column
780 concentrations are mainly over most continental areas in the middle and low latitudes.
781 The SOA mainly includes biogenic SOA, anthropogenic SOA, and semi-volatile SOA.
782 The differences of SOA are mainly due to the higher BVOCs emissions and higher OH
783 levels in MOZART-4x than in CB05_GE. Different branching ratios used in MOZART-

784 4x and CB05_GE can also contribute to the different SOA predictions. MOZART-4x
785 includes explicit species and more types of precursors for alkylperoxy radicals (RO_2), and
786 different reaction rate constants for different reactions, whereas in CB05_GE, all oxidized
787 VOCs are lumped as one species (i.e., RO_2) and branching ratios are estimated based on
788 the only three reactions (i.e., reactions of RO_2 with NO, HO_2, and RO_2). These
789 differences can contribute to the differences in the estimation of branching ratios, and
790 therefore, affect the partitioning between organic gas and aerosols through the 1.5 D VBS
791 treatment implemented in CAM5-NCSU.
792
793 **5.2 SOA Comparisons**
794 Figure 9 shows the contributions to total SOA (TSOA) concentrations from
795 anthropogenic sources (ASOA), biogenic sources (BSOA), glyoxal (GLSOA), and semi-
796 volatile organic aerosol (SVSOA) over Australia, Europe, North America, South Africa,
797 South America, and East Asia over 2008-2010. The contributions of ASOA to TSOA
798 predicted by MOZART-4x and CB05_GE are about 17-44%, and 10-47%, respectively,
799 with South America the least and East Asia the most. The contributions of BSOA to
800 TSOA predicted by MOZART-4x and CB05_GE are about 31-75%, and 26-76%,
801 respectively, with East Asia the least and South America the most. The contribution of
802 GLSOA to TSOA predicted by CB05_GE is about 2-6%. CB05_GE used in this work
803 includes a simple conversion of glyoxal to condensable VOCs, which can be uptaken by

804 preexisting particles to form SOA. However, this conversion is not included in
805 MOZART-4x. Therefore, there is no GLSOA predicted by MOZART-4x despite it
806 predicts higher glyoxal as shown in Figure 3. The contributions of SVSOA to TSOA
807 predicted by MOZART-4x and CB05_GE are about 8-37%, and 8-41%, respectively, with
808 South America the least and South Africa the most. Among four types of SOA, both
809 MOZART-4x and CB05_GE predict BSOA as the main contributor over most regions
810 (e.g., Australia, North America, South Africa, and South America) and ASOA as the main
811 contributor over East Asia, which is mainly due to the much higher anthropogenic
812 emissions over East Asia. Europe is a different example. MOZART-4x predicts BSOA as
813 the top contributor (44%) and ASOA as the second largest contributor (40%), whereas
814 CB05_GE predicts ASOA as the top contributor (45%) and BSOA as the second largest
815 contributor (36%). Both MOZART-4x and CB05_GE predict ASOA as the top
816 contributor (46-59%) for spring, fall, and winter, and BSOA as the top contributor (57%
817 and 47%, respectively) for summer over Europe. Since MOZART-4x predicts higher
818 BSOA than CB05_GE, BSOA is dominant in MOZART-4x on the annual average. The
819 higher BSOA from MOZART-4x than CB05_GE is mainly due to the higher BVOCs
820 emissions in MOZART-4x and higher OH levels in MOZART-4x. The total BVOCs
821 emission in MOZART-4x is about 2.5×10^{-3} kg m^{-2} yr^{-1}, which is about 7.2×10^{-5} kg m^{-2} yr^{-1} (or 2.9%) higher than CB05_GE. The higher BVOCs emissions in MOZART-4x are
822
823 mainly due to the different species mapping for MEGAN emission calculations. The

differences of SOA from biogenic alkenes between MOZART-4x and CB05_GE are MYRC and BCARY in MOZART-4x, and OCI, HUM, and TER in CB05_GE (as shown in Table 1). In CAM-chem that uses MOZART, MEGAN calculates all of the individual species and CAM-chem sums them up to map with the MOZART mechanism species. For example, MYRC emissions consist of myrcene and ocimene, BCARY emissions consist of beta-caryophyllene, alpha-bergamotene, beta-bisabolene, beta-farnescene, and alpha-humulene, and LIMON emissions consist of limonene, phellandrene, and terpinene. Therefore, the biogenic emissions for more types of VOCs in MOZART-4x are higher than those in CB05_GE, resulting in higher BSOA in MOZART-4x. The differences in SOA from aromatics between MOZART-4x and CB05_GE are BENZENE in MOZART-4x and PAH in CB05_GE (as shown in Table 1). The emissions of PAH are higher over Europe, East Asia, eastern U.S., and South Africa. The benzene emissions are about 1 order of magnitude higher than the emissions of PAH, and the rate constant of the oxidation of benzene by OH is temperature dependent whereas it is constant for oxidation of PAH by OH. In addition, OH levels are higher in MOZART-4x than those in CB05_GE. These differences could result in different ASOA between two simulations. Both MOZART-4x and CB05_GE predict higher SVSOA contributions over South Africa than other regions, which is mainly due to the higher POA emissions (e.g., biomass burning) over this region.

Although the percentage contributions of different types of SOA predicted by

MOZART-4x and CB05_GE are similar over most regions, the absolute mass concentrations of different types of SOA are different. For example, TSOA predicted by MOZART-4x is about 0.02-2.0 mg m^{-2} higher than by CB05_GE over these regions. ASOA predicted by MOZART-4x is about 0.068-1.017 mg m^{-2} higher than predicted by CB05_GE over most regions except Europe (0.054 mg m^{-2} lower) and East Asia (0.062 mg m^{-2} lower). BSOA predicted by MOZART-4x is about 0.162-1.365 mg m^{-2} higher than predicted by CB05_GE over most regions except Australia (0.003 mg m^{-2} lower). MOZART-4x includes SOA formation from benzene, which can predict higher ASOA formation. In addition, OH predicted by MOZART-4x is higher than CB05_GE (See Figure 8a), which can produce more condensable SOA gaseous precursors through oxidations of VOCs. The higher BVOCs emissions in MOZART-4x due to different mapping for MEGAN species can also contribute to the higher BSOA formation in MOZART-4x.

Both MOZART-4x and CB05_GE predict POA burdens of 0.36 Tg, which is about 0.1 Tg lower than those by Shrivastava et al. (2015), indicating that POA may be too volatile with the current implementation of VBS SOA in CESM/CAM5 and possible lower POA emissions used in this work. MOZART-4x predicts SOA burden of 1.82 Tg, which is slightly higher (by 0.05 Tg) than that predicted by Shrivastava et al. (2015). This can be attributed to different emissions used in CESM/CAM5 and Shrivastava et al. (2015), as well as differences in the model treatment for SOA formation in both work.

For example, nine volatility bines are used in this work to represent the aging and gas-particle partitioning of POA, instead of five volatility bins used in Shrivastava et al. (2015). In addition, compared to the reaction (3) in Shrivastava et al. (2015), the remaining mass is assumed to be lost to a species with a volatility higher than the volatility values in the VBS structure, instead of being oxidized to form CO/CO_2.

6. Conclusions

In this work, MOZART-4x and CB05_GE are coupled with CAM5-NCSU. MOZART-4x uses lumped species approach to represent organic chemistry whereas CB05_GE uses lumped structure approach. MOZART-4x and CB05_GE include different surrogates for SOA precursors, which can result in different SOA predictions. MOZART-4x includes HO_x recycling associated with improved isoprene chemistry whereas CB05_GE contains simpler isoprene chemistry, which can result in different OH and isoprene predictions and thus, SOA predictions. CB05_GE includes additional oxidation of SO_2 by O_3 over the surface of dust particles to produce additional SO_4^{2-}, which is not included in MOZART-4x. These differences can result in different secondary gas and aerosols predictions.

The comparisons between the two gas-phase mechanisms are conducted in terms of chemical and cloud/radiative predictions. Predictions of major gases and inorganic aerosols predicted by MOZART-4x and CB05_GE are overall similar. Significant

884 differences in some species (e.g., NO_y, glyoxal, and SOA) predictions are mainly due to
885 the different reaction pathways treated in the two mechanisms. Large biases exist for
886 surface SO_2, CO, NH_3, $PM_{2.5}$ and PM_{10} predictions against available observations, which
887 is likely due to the uncertainties in the emissions or emission injection heights. Several
888 studies indicate that the uncertainties in regional emissions (e.g., BC and SO_2) can be
889 expected to be as large as a factor of 2 or larger (Bond et al., 2007; Smith et al., 2011).
890 Large discrepancies still remain for major species such as SO_2, NO_x, BC, and CO among
891 different inventories (Granier et al., 2011). Both surface CO mixing ratios and column
892 CO mass abundances are underpredicted, which is mainly due to underestimations in the
893 CO emissions from biomass burning and possible uncertainties in the OH production.
894 Surface SO_2 mixing ratio is overpredicted whereas column SO_2 abundance is
895 underpredicted, indicating the uncertainties in the vertical mixing scheme or emission
896 injection heights as reported in East Asia (Zhang et al., 2015a, b), as well as satellite
897 retrievals. For example, Lee et al. (2009) found that there is an overall error in the annual
898 SO_2 retrievals of 45-80% over polluted regions, especially over eastern China.
899 Uncertainties in online dust and sea-salt emissions can also result in inaccurate
900 predictions in $PM_{2.5}$ and PM_{10}. Both MOZART-4x and CB05_GE overpredict surface O_3
901 over CONUS, Europe, and East Asia, which is due in part to less O_3 titration resulted
902 from underpredictions of NO_x, the dilution of NO_x emissions resulted from the use of a
903 coarse grid resolution, as well as uncertainties in the O_3 dry deposition simulated in the

model.

The concentration of OC over CONUS is well predicted by MOZART-4x, with an NMB of 2.1%, whereas it is moderately underpredicted by CB05_GE, with an NMB of -20.7%. Compared to the observations at the four sites in the U.S. from Lewandowski et al. (2013), SOA is well predicted by MOZART-4x, with an NMB of -1.9%, whereas it is moderately underpredicted by CB05_GE, with an NMB of -23.1%, indicating a better capability to predict SOA over these sites by MOZART-4x despite its tendency to overpredict SOA concentrations at sites with low SOA levels such as Bakersfield and Pasadena, CA. However, the concentrations of OC over Europe are largely underpredicted by both MOZART-4x and CB05_GE, with NMBs of -74.2% and -75.1%, respectively, indicating the uncertainties in the emissions, chemical reactions, as well as SOA formation treatment. The different AOD predictions between CB05_GE and MOZART-4x are mainly due to different predictions in SOA, SO_4^{2-}, NH_4^+, NO_3^-, and dust concentrations.

The cloud/radiative predictions from the two simulations are also similar, with slightly better domain average performance of CCN5, LWP, and LWCF in CB05_GE. But MOZART-4x predicts slightly better CCN profile over Beijing than CB05_GE compared to aircraft measurements. The different gas-phase mechanisms result in different predictions in aerosols and clouds, and therefore, a domain average difference of 0.5 W m^{-2} in simulated SWCF, which can be as large as 13.6 W m^{-2} over subtropical

924 regions.

925 In summary, MOZART-4x and CB05_GE differ in their approaches to represent
926 VOCs and surrogates for SOA precursors. MOZART-4x includes a more detailed
927 representation of isoprene chemistry compared to CB05_GE. Based on the above
928 comparisons of simulations using both mechanisms and evaluation against available
929 measurements in this study, MOZART-4x with the 1.5 D VBS SOA module in CESM-
930 NCSU generally gives a better agreement with observations for surface concentrations of
931 O_3 over Europe, HNO_3, HCHO, ISOP over CONUS, SOA, SO_4^{2-}, NO_3^-, and NH_4^+ over
932 CONUS and Europe, and column mass abundances of HCHO, $C_2H_2O_2$, SO_2, and O_3,
933 whereas CB05_GE generally gives a better agreement for surface concentrations of SO_2,
934 NH_3, O_3 over CONUS and East Asia, HNO_3 over Europe, $PM_{2.5}$ and PM_{10} over Europe,
935 PM_{10} over East Asia, vertical profiles of NO_y, and column mass abundances of CO. Both
936 simulations give predictions of cloud/radiative variables with slightly better domain
937 average performance of CCN5, LWP, and LWCF in CB05_GE.

938 **7. Code and Data Availability**

939 The results in this paper are based on output from simulations performed with the
940 NCAR Community Earth System Model (CESM) version 1.2.2
941 (https://www2.cesm.ucar.edu/models/current) with additional model development and
942 modifications by the Air Quality Forecasting Laboratory, North Carolina State University,
943 Raleigh, NC, U.S.A. The added codes have been provided to NCAR for potential future

944 release to NCAR for community use. Upon request, we can provide the inputs, the
945 namelist file, a brief instruction, and sample output for a 1-day test case.

946 **Acknowledgments**

947 This work is sponsored by the U.S. National Science Foundation EaSM program AGS-
948 1049200 and NCAR Advanced Study Program. MODIS data and CERES data are
949 provided by NASA via http://ladsweb.nascom.nasa.gov/data/search.html and
950 http://ceres.larc.nasa.gov/order_data.php, respectively. CDNC data are provided by Ralf
951 Bennartz. Other surface network data were downloaded from their respective web sites.
952 ARCPAC and CalNex data are from NOAA, STRAT08 data are from NCAR, ARCTAS
953 data are from NASA, CCN_China are from Zhang et al. (2011), and SOA data of
954 Lewandowski et al. (2013) are provided by Tadeusz Kleindienst, U.S. EPA. We would
955 like to acknowledge high-performance computing support from Yellowstone
956 (ark:/85065/d7wd3xhc) provided by NCAR's Computational and Information Systems
957 Laboratory, sponsored by the U.S. National Science Foundation. The National Center for
958 Atmospheric Research is operated by the University Corporation for Atmospheric
959 Research with funding from the National Science Foundation.

960

961 **References**

962 Aghedo, A. M., Bowman, K. W., Worden, H. M., Kulawik, S. S., Shindell, D. T.,
963 Lamarque, J.-F., Faluvegi, G., Parrington, M., Jones, D. B. A., and Rast, S.: The
964 vertical distribution of ozone instantaneous radiative forcing from satellite and

chemistry climate models, J. Geophys. Res., 116, D01305, doi:10.1029/2010JD014243, 2011.

Barahona, D., West, R. E. L., Stier, P., Romakkaniemi, S., Kokkola, H., and Nenes, A.: Comprehensively accounting for the effect of giant CCN in cloud activation parameterizations, Atmos. Chem. Phys., 10(5), 2467-2473, doi:10.5194/acp-10-2467-2010, 2010.

Bennartz, R.: Global assessment of marine boundary layer cloud droplet number concentration from satellite, J. Geophys. Res., 112, D02201, doi: 10.1029/2006JD007547, 2007.

Boersma, K. F., Eskes, H. J., and Brinksma E. J.: Error analysis for tropospheric NO_2 retrieval from space, J. Geophys. Res., 109, D04311, doi:10.1029/2003JD003962, 2004.

Bond, T. C., Bhardwaj, E., Dong, R., Jogani, R., Jung, S., Roden, C., Streets, D. G., and Trautmann, N. M.: Historical emissions of black and organic carbon aerosol from energy-related combustion, 1850-2000, Global Biogeochem. Cy., 21, GB2018, doi:10.1029/2006GB002840, 2007.

Brock, C. A., Cozic, J., Bahreini, R., Froyd, K. D., Middlebrook, A. M., McComiskey, A., Brioude, J., Cooper, O. R., Stohl, A., Aikin, K. C., de Gouw, J. A., Fahey, D. W., Ferrare, R. A., Gao, R.-S., Gore, W., Holloway, J. S., Hübler, G., Jefferson, A., Lack, D. A., Lance, S., Moore, R. H., Murpphy, D. M., Nenes, A., Novelli, P. C., Nowak, J. B., Ogren, J. A., Peischl, J., Pierce, R. B., Pilewskie, P., Quinn, P. K., Ryerson, T. B., Schmidt, K. S., Schwarz, J. P., Sodemann, H., Spackman, J. R., Stark, H., Thomson, D. S., Thornberry, T., Veres, P., Watts, L. A., Warneke, C., and Wollny, A. G.: Characteristics, sources, and transport of aerosols measured in spring 2008 during the aerosol, radiation, and cloud processes affecting Arctic Climate (ARCPAC) Project, Atmos. Chem. Phys., 11, 2423-2453, doi:10.5194/acp-11-2423-2011, 2011.

Cappa, C. D. and Jimenez, J. L.: Quantitative estimates of the volatility of ambient organic aerosol, Atmos. Chem. Phys., 10, 5409-5424, doi:10.5194/acp-10-5409-2010, 2010.

Chan, A. W. H., Kautzman, K. E., Chhabra, P. S., Surratt, J. D., Chan, M. N., Crounse, J. D., Kürten, A., Wennberg, P. O., Flagan, R. C., and Seinfeld, J. H.: Secondary organic aerosol formation from photooxidation of naphthalene and alkylnaphthalens: implications for oxidation of intermediate volatility organic compounds (IVOCs), Atmos. Chem. Phys., 9, 3049-3060, 2009.

Couvidat, F., Kim, Y., Sartelet, K., Seigneur, C., Marchand, N., and Sciare, J.: Modeling secondary organic aerosol in an urban area: application to Paris, France, Atmos. Chem. Phys., 13, 983-996, 2013.

Emmons, L. K., Walters, S., Hess, P. G., Lamarque, J.-F., Pfister, G. G., Fillmore, D., Granier, C., Guenther, A., Kinnison, D., Laepple, T., Orlando, J., Tie, X., Tyndall, G., Wiedinmyer, C., Baughcum, S. L., and Kloster, S.: Description and evaluation of the Model for Ozone and Related chemical Tracers, version 4 (MOZART-4), Geosci. Model Dev., 3, 43-67, doi:10.5194/gmd-3-43-2010, 2010.

Fountoukis, C. and Nenes, A.: Continued Development of a Cloud Droplet Formation Parameterization for Global Climate Models, J. Geoph. Res., 110, D11212, doi:10.1029/2004JD005591, 2005.

Fountoukis, C and Nenes, A.: ISORROPIA II: a computationally efficient thermodynamic equilibrium model for K^+- Ca^{2+} -Mg^{2+} -NH_4^+ -Na^+-SO_4^{2-}-NO_3^--Cl^--H_2O aerosols, Atmos. Chem. Phys., 7, 4639-4659, doi:10.5194/acp-7-4639-2007, 2007.

Gantt, B., He, J., Zhang, X., Zhang, Y., and Nenes, A.: Incorporation of advanced aerosol activation treatments into CESM/CAM5: model evaluation and impacts on aerosol indirect effects, Atmos. Chem. Phys., 14, 7485-7497, doi:10.5194/acp-14-7485-2014.

Gery, M. W., Whitten, G. Z., Killus, J. P., and Dodge, M. C.: A photochemical kinetics mechanism for urban and regional scale computer modeling, J. Geophys. Res., 94(D10), 12,925-12,956, doi:10.1029/JD094iD10p12925, 1989.

Glotfelty, T., He, J., and Zhang, Y.: Updated organic aerosol treatments in CESM/CAM5: development and initial application, in preparation, 2015.

Granier, C., Bessagnet, B., Bond, T., D'Angiola, A., Denier van der Gon, H., Frost, G. J., Heil, A., Kaiser, J. W., Kinne, S., Klimont, Z., Kloster, S., Lamarque, J.-F., Liousse, C., Masui, T., Meleux, F., Mieville, A., Ohara, T., Raut, J.-C., Riahi, K., Schultz, M. G., Smith, S. J., Thompson, A., van Aardenne, J., van der Werf, G. R., and van Vuuren, D. P.: Evolution of anthropogenic and biomass burning emissions of air pollutants at global and regional scales during the 1980-2010 period, Climatic Change, 109, 163-190, doi:10.1007/s10584-011-0154-1, 2011.

Guenther, A. B., Jiang, X., Heald, C. L., Sakulyanontvittaya, T., Duhl, T., Emmons, L. K., and Wang, X.: The Model of Emissions of Gases and Aerosols from Nature version 2.1 (MEGAN2.1): an extended and updated framework for modeling biogenic emissions, Geosci. Model Dev., 5, 1471-1492, doi:10.5194/gmd-5-1471-2012, 2012.

1033 He, J. and Zhang, Y.: Improvement and further development in CESM/CAM5: gas-phase
1034 chemistry and inorganic aerosol treatments, Atmos. Chem. Phys., 14, 9171-9200,
1035 doi:10.5194/ acp-14-9171-2014, 2014.

1036 He, J., Zhang, Y., Glotfelty, T., He, R., Bennartz, R., Rausch, J., and Sartelet, K.: Decadal
1037 simulation and comprehensive evaluation of CESM/CAM5.1 and advanced
1038 chemistry, aerosol microphysics, and aerosol-cloud interactions, J. Adv. Model. Earth
1039 Syst., 7, 110-141, doi: 10.1002/2014MS000360, 2015.

1040 Hodzic, A., Jimenez, J. L., Madronich, S., Canagaratna, M. R., DeCarlo, P. F., Kleinman,
1041 L., and Fast, J.: Modeling organic aerosols in a mega-city: Potential contribution of
1042 semi-volatile and intermediate volatility primary organic compounds to secondary
1043 organic aerosol formation, Atmos. Chem. Phys., 10(12), 5491-5514,
1044 doi:10.5194/acp-10-5491-2010, 2010.

1045 IPCC: Climate Change 2013: The Physical Science Basis. Contribution of Working
1046 Group I to the Fifth Assessment Report of the Intergovernmental Panel on Climate
1047 Change [Stocker, T.F., D. Qin, G.-K. Plattner, M. Tignor, S.K. Allen, J. Boschung, A.
1048 Nauels, Y. Xia, V. Bex and P.M. Midgley (eds.)]. Cambridge University Press,
1049 Cambridge, United Kingdom and New York, NY, USA, 1535 pp,
1050 doi:10.1017/CBO9781107415324, 2013.

1051 Jacob, D. J., Crawford, J. H., Maring, H., Clarke, A. D., Dibb, J. E., Emmons, L. K.,
1052 Ferrare, R. A., Hostetler, C. A., Russell, P. B., Singh, H. B., Thompson, A. M., Shaw,
1053 G. E., McCauley, E., Pederson, J. R., and Fisher, J. A.: The Arctic Research of the
1054 Composition of the Troposphere from Aircraft and Satellites (ARCTAS) mission:
1055 design, execution, and first results, Atmos. Chem. Phys., 10, 5191-5212,
1056 doi:10.5194/acp-10-5191-2010, 2010.

1057 Jacob, D. J. and Winner, D. A.: Effect of climate change on air quality, Atmos. Environ.,
1058 43, 51-63, 2009.

1059 Jathar, S. H., Farina, S. C., Robinson, A. L., and Adams, P. J.: The influence of semi-
1060 volatile and reactive primary emissions on the abundance and properties of global
1061 organic aerosol, Atmos. Chem. Phys., 11, 7727-7746, doi:10.5194/acp-11-7727-2011,
1062 2011.

1063 Jimenez, J. L., Canagaratna, M. R., Donahue, N. M., Prevot, A. S. H., Zhang, Q., Kroll, J.
1064 H., DeCarlo, P. F., Allan, J. D., Coe, H., Ng, N. L., Aiken, A. C., Docherty, K. S.,
1065 Ulbrich, I. M., Grieshop, A. P., Robinson, A. L., Duplissy, J., Smith, J. D., Wilson, K.
1066 R., Lanz, V. A., Hueglin, C., Sunn, Y. L., Tian, J., Laaksonen, A., Raatikainen, T.,
1067 Rautiainen, J., Vaattovaara, P., Ehn, M., Kulmala, M., Tomlinson, J. M., Collins, D.

1068 R., Cubison, M. J., Dunlea, E., J., Huffman, J. A., Onaasch, T. B., Alfarra, M. R.,
1069 Williams, P. I., Bower, K., Kondo, Y., Schneider, J., Drewnick, F., Borrmann, S.,
1070 Weimer, S., Demerjian, K., Salcedo, D., Cottrell, L., Griffin, R., Takami, A.,
1071 Miyoshi, T., Hatakeyama, S., Shimono, A., Sun, J. Y., Zhang, Y. M., Dzepina, K.,
1072 Kimmel, J. R., Sueper, D., Jayne, J. T., Herndon, S. C., Trimborn, A. M., Williams, L.
1073 R., Wood, E. C., Middlebrook, A. M., Kolb, C. E., Baltensperger, U., Worsnop, D.
1074 R.: Evolution of organic aerosols in the atmosphere, Science, 326, 1525-1529,
1075 doi:10.1126/science.1180353, 2009.

1076 Karamchandani, P., Zhang, Y., Chen, S.-Y., and Balmori-Bronson, R.: Development of an
1077 extended chemical mechanism for global-through-urban applications, Atmospheric
1078 Pollution Research, 3, 1-24, 2012.

1079 Kay, J. E., Hillman, B. R., Klein, S. A., Zhang, Y., Medeiros, B., Pincus, R., Gettelman,
1080 A., Eaton, B., Boyle, J., Marchand, R., and Ackerman, T. P.: Exposing global cloud
1081 biases in the Community Atmosphere Model (CAM) using satellite observations and
1082 their corresponding instrument simulators, J. Climate, 25, 5190-5207,
1083 doi:10.1175/JCLI-D-11-00469.1, 2012.

1084 Kim Y., Sartelet, K., and Seigneur C.: Comparison of two gas-phase chemical kinetic
1085 mechanisms of ozone formation over Europe, J. Atmo. Chem., 62, 89-119,
1086 DOI10.1007/s10874-009-9142-5, 2009.

1087 Kim, Y., Sartelet, K., and Seigneur, C.: Formation of secondary aerosols: impact of the
1088 gas-phase chemical mechanism, Atmos. Chem. Phys. 11, 583-598, doi:10.5194/acp-
1089 11-583-2011, 2011a.

1090 Kim, Y., Couvidat, F., Sartelet, K., and Seigneur, C.: Comparison of Different Gas-Phase
1091 Mechanisms and Aerosol Modules for Simulating Particulate Matter Formation, J. of
1092 Air & Waste Management Association, 61, 1218-1226,
1093 doi:10.1080/10473289.2011.603999, 2011b.

1094 Kinnison, D. E., Brasseur, G. P., Walters, S., Garcia, R. R., Marsh, D. A., Sassi, F.,
1095 Boville, B. A., Harvey, L., Randall, C., Emmons, L., Lamarque, J.-F., Hess, P.,
1096 Orlando, J., Tyndall, G., Tie, X. X., Randel, W., Pan, L., Gettelman, A., Granier, C.,
1097 Diehl, T., Niemeier, U., and Simmons, A. J.: Sensitivity of chemical tracers to
1098 meteorological parameters in the MOZART-3 chemical transport model, J. Geophys.
1099 Res., 112, D20302, doi:10.1029/2006JD007879, 2007.

1100 Knote, C., Tuccella, P., Curci, G., Emmons, L., Orlando, J. J., Madronich, S., Baró, R.,
1101 Jiménez-Guerrero, P., Luecken, D., Hogrefe, C., Forkel, R., Werhahn, J., Hirtl, M.,
1102 Pérez, J. L., San José, R., Giordano, L., Brunner, D., Khairunnisa, Y., and Zhang, Y.:

1103 Influence of the choice of gas-phase mechanism on predictions of key gaseous
1104 pollutants during the AQMEII phase-2 intercomparison, Atmos. Environ.,
1105 http://dx.doi.org/10.1016/j.atmosenv.2014.11.066, 2014a.

1106 Knote, C., Hodzic, A., Jimenez, J. L., Volkamer, R., Orlando, J. J., Baidar, S., Brioude, J.,
1107 Fast, J. Gentner, D. R., Goldstein, A. H., Hayes, P. L., Knighton, W. B., Oetjen, H.,
1108 Setyan, A., Stark, H., Thalman, R., Tyndall, G., Washenfelder, R., Waxman, E., and
1109 Zhang, Q.: Simulation of semi-explicit mechanisms of SOA formation from glyoxal
1110 in aerosol in a 3-D model, Atmos. Chem. Phys., 14, 6213-6239, doi:10.5194/acp-14-
1111 6213-2014, 2014b.

1112 Kumar, P., Sokolik, I. N., and Nenes, A.: Parameterization of cloud droplet formation for
1113 global and regional models: including adsorption activation from insoluble CCN,
1114 Atmos. Chem. Phys., 9, 2517-2532, doi:10.5194/acp-9-2517-2009, 2009.

1115 Lamarque, J.-F., Bond, T. C., Eyring, V., Granier, C., Heil, A., Klimont, Z., Lee, D.,
1116 Liousse, C., Mieville, A., Owen, B., Schultz, M. G., Shindell, D., Smith, S. J.,
1117 Stehfest, E., Van Aardenne, J., Cooper, O. R., Kainuma, M., Mahowald, N., Mc-
1118 Connell, J. R., Naik, V., Riahi, K., and van Vuuren, D. P.: Historical (1850-2000)
1119 gridded anthropogenic and biomass burning emissions of reactive gases and aerosols:
1120 methodology and application, Atmos. Chem. Phys., 10, 7017-7039, doi:10.5194/acp-
1121 10-7017-2010, 2010.

1122 Lamarque, J. F., Emmons, L. K., Hess, P. G., Kinnison, D. E., Tilmes, S., Vitt, F., Heald,
1123 C. L., Holland, E. A., Lauritzen, P. H., Neu, J., Orlando, J. J., Rasch, P. J., and
1124 Tyndall, G. K.:CAM-chem: description and evaluation of interactive atmospheric
1125 chemistry in CESM, Geosci. Model Dev., 5, 369-411, doi:10.5194/gmd-5-369-2012,
1126 2012.

1127 Lamarque, J.-F., McConnell, J. R., Shindell, D. T., Orlando, J. J., and Tyndall, G. S.:
1128 Understanding the drivers for the 20th century change of hydrogen peroxide in
1129 Antarctic ice-cores, Geophys. Res. Lett., 38, L04810, doi:10.1029/2010GL045992,
1130 2011a.

1131 Lamarque, J.-F., Kyle, G. P., Meinshausen, M., Riahi, K., Smith, S. J., van Vuuren, D. P.,
1132 Conley, A., and Vitt, F.: Global and regional evolution of short-lived radiatively-
1133 active gases and aerosols in the Representative Concentration Pathways, Climatic
1134 Change, 109, 191-212, 2011b.

1135 Lamarque, J.-F., Kinnison, D. E., Hess, P. G., and Vitt, F.: Simulated lower stratospheric
1136 trends between 1970 and 2005: identifying the role of climate and composition
1137 changes, J. Geophys. Res., 113, D12301, doi:10.1029/2007JD009277, 2008.

1138 Lamarque, J. F., Shinedell, D. T., Josse, B., Young, P. J., Cionni, I., Eyring, V.,
1139 Bergmann, D., Cameron-Smith, P., Collins, W. J., Doherty, R., Dalsoren, S.,
1140 Faluvegi, G., Folberth, G., Ghan, S. J., Hiriwutz, L. W., Lee, Y. H., MacKenzie, I.
1141 A., Nagashima, T., Naik, V., Plummer, D., Righi, M., Rumbold, S. T., Schulz, M.,
1142 Skeie, R. B., Stevenson, D. S., Strode, S., Sudo, K., Szopa, S., Voulgarakis, A., and
1143 Zeng, G.: The atmospheric chemistry and climate model intercomparison project:
1144 overview and description of models, simulations and climate diagnostics, Geosci.
1145 Model Dev., 6, 179-206, doi:10.5194/gmd-6-179-2013, 2013.

1146 Lamarque, J.-F. and Solomon, S.: Impact of Changes in Climate and Halocarbons on
1147 Recent Lower Stratosphere Ozone and Temperature Trends, J. Climate, 23, 2599-
1148 2611, 2010.

1149 Lee, C., Martin, R. V., Donkelaar, A. van, O'Byrne, G., Krotkov, N., Richter, A., Huey, L.
1150 G., and Holloway, J. S.: Retrieval of vertical columns of sulfur dioxide from
1151 SCIAMACHY and OMI: Air mass factor algorithm development, validation, and
1152 error analysis, J. Geophys. Res., 114, D22303, doi:10.1029/2009JD012123,
1153 2009.Levy, R. C., Mattoo, S., Munchak, L. A., Remer, L. A., Sayer, A. M., Patadia,
1154 F., and Hsu, N. C.: The Collection 6 MODIS aerosol products over land and ocean,
1155 Atmos. Meas. Tech., 6, 2989–3034, doi:10.5194/amt-6-2989-2013, 2013.

1156 Lewandowski, M., Piletic, I. R., Kleindienst, T. E., Offenberg, J. H., Beaver, M. R., Jaoui,
1157 M., Docherty, K. S., and Edney, E. O.: Secondary organic aerosol characterization at
1158 field sites across the United States during the spring-summer period, Int. J. Environ.
1159 An. Ch., 93, 1084-1103, 2013.

1160 Liu, X., Easter, R. C., Ghan, S. J., Zaveri, R., Rasch, P., Shi, X., Lamarque, J.-F.,
1161 Gettleman, A., Morrison, H., Vitt, F., Conley, A., Park, S., Neale, R., Hannay, C.,
1162 Ekman, A. M. L., Hess, P., Mahowald, N., Collins, W., Iacono, M.J., Bretherton, C.
1163 S., Flanner, M. G., and Mitchell, D.L.: Toward a minimal representation of aerosols
1164 in climate models: description and evaluation in the Community Atmosphere Model
1165 CAM5, Geosci. Model Dev., 5, 709-739, 2012.

1166 Liu, X., Zhang, Y., Cheng, S.-H., Xing, J., Zhang, Q., Streets, D. G., Jang, C., Wang, W.-
1167 X., and Hao, J.-M.: Understanding of regional air pollution over China using CMAQ,
1168 partI: performance evaluation and seasonal variation, Atmos. Environ., 44 (2010),
1169 pp. 2415-2426, http://dx.doi.org/10.1016/j.atmosenv.2010.03.035.

1170 Luecken, D. J., Phillips, S., Sarwar, G., and Jang, C.: Effects of using the CB05 vs.
1171 SAPRC99 vs. CB4 chemical mechanism on model predictions: Ozone and gas-phase

photochemical precursor concentrations, Atmos. Environ., 42, 5805-5820, doi:10.1016/j.atmosenv.2007.08.056, 2008.

Ma, P.-L., Rasch, P. J., Wang, H., Zhang, K., Easter, R. C., Tilmes, S., Fast, J. D., Liu, X., Yoon, J.-H., and Lamarque, J.-F.: The role of circulation features on black carbon transport into the Arctic in the Community Atmosphere Model version 5 (CAM5), J. Geophys. Res. Atmos., 118, 4657-4669, doi:10.1002/jgrd.50411, 2013.

Martensson, E. M., Nilsson, E. D., deLeeuw, G., Cohen, L. H., and Hansson, H. C.: Laboratory simulations and parameterization of the primary marine aerosol production, J. Geophys. Res., 108(D9), 4297, doi:10.1029/2002JD002263, 2003.

Martin, M. V., Heald, C. L., and Arnold, S. R.: Coupling dry deposition to vegetation phenology in the Community Earth System Model: Implications for the simulation of surface O_3, Geophys. Res. Lett., 41, 2988-2996, doi:10.1002/2014GL059651, 2014.

May, A. A., Presto, A. A., Hennigan, C. J., Nguyen, N. T., Gordon, T. D., and Robinson, A. I.: Gas-particle partitioning of primary organic aerosol emissions: (1), gasoline vehicle exhaust, Atmos. Environ., 77, 128-139, doi:10.1016/j.atmosenv.2013.04.060, 2013a.

May, A. A., Levin, E. J. T., Hennigan, C. J., Riipinen, I., Lee, T., Collett Jr., J. L., Jimenez, J. L., Kreidenweis, S. M., and Robinson, A. L.: Gas-particle partitioning of primary organic aerosol emissions: 3. Biomass burning, J. Geophys. Res. Atmos., 118, 11,327-11,338, doi:10.1002/jgrd.50828, 2013b.

Meinshausen, M., Smith, S. J., Calvin, K., Daniel, J. S., Kainuma, M. L. T., Lamarque, J.-F., Matsumoto, K., Montzka, S., Raper, S., Riahi, K., Thomson, A., Velders, G. J. M., and van Vuuren, D. P.: The RCP Greenhouse gas concentrations and their extensions from 1765 to 2300, Climatic Change, 109, 213-241, 2011.

Merikanto, J., Napari, I., Vehkamaki, H., Anttila, T., and Kulmala, M.: New parameterization of sulfuric acid-ammonia-water ternary nucleation rates at tropospheric conditions, J. Geophys. Res., 112, D15207, doi: 10.1029/2006JD007977, 2007.

Naik, V., Voulgarakis, A., Fiore, A. M., Horowitz, L. W., Lamarque, J.-F., Lin, M., Prather, M. J., Young, P. J., Bergmann, D., Cameron-Smith, P. J., Cionni, I., Collins, W. J., Dalsøren, S. B., Doherty, R., Eyring, V., Faluvegi, G., Folberth, G. A., Josse, B., Lee, Y. H., MacKenzie, I. A., Nagashima, T., van Noije, T. P. C., Plummer, D. A., Righi, M., Rumbold, S. T., Skeie, R., Shindell, D. T., Stevenson, D. S., Strode, S., Sudo, K., Szopa, S., and Zeng, G.: Preindustrial to present-day changes in

tropospheric hydroxyl radical and methane lifetime from the Atmospheric Chemistry and Climate Model Intercomparison Project (ACCMIP), Atmos. Chem. Phys., 13, 5277-5298, doi:10.5194/acp-13-5277-2013, 2013.

Pan, L. L., Bowman, K. P., Atlas, E. L., Wofsy, S. C., Zhang, F., Bresch, J. F., Ridley, B. A., Pittman, J. V., Homeyer, C. R., Romashkin, P., and Cooper, W. A.: The stratosphere-troposphere analyses of regional transport 2008 (START08) experiment, Bull. Am. Meteorol. Soc., 91, 327-342, 2010.

Price, C. and Rind, D.: A simple lightning parameterization for calculating global lightning distributions, J. Geophys. Res., 97, 9919-9933, doi:10.1029/92JD00719, 1992.

Price, C., Penner, J., and Prather, M.: NO_x from lightning 1, Global distribution based on lightning physics, J. Geophys. Res., 102, 5929-5941, 1997.

Reutter, P., Su, H., Trentmann, J., Simmel, M., Rose, D., Gunthe, S. S., Wernli, H., Andreae, M. O., and Pöschl, U.: Aerosol- and updraft-limited regimes of cloud droplet formation: influence of particle number, size and hygroscopicity on the activation of cloud condensation nuclei (CCN), Atmos. Chem. Phys., 9, 7067-7080, doi:10.5194/acp-9-7067-2009, 2009.

Robinson, A. L., Donahue, N. M., Shrivastava, M. K., Weitkamp, E. A., Sage, A. M., Grieshop, A. P., Lane, T. E., Pierce, J. R., and Pandis, S. N.: Rethinking organic aerosols: Semivolatile emissions and photochemical aging, Science, 315, 1259-1262, doi:10.1126/science.1133061, 2007.

Ryerson, T. B., Andrews, A. E., Angevine, W. M., Bates, T. S., Brock, C. A., Cairns, B., Cohen, R. C., Cooper, O. R., de Gouw, J. A., Fehsenfeld, F. C., Ferrare, R. A., Fischer, M. L., Flagan, R. C., Goldstein, A. H., Hair, J. W., Hardesty, R. M., Hostetler, C. A., Jimenez, J. L., Langford, A. O., McCauley, E., McKeen, S. A., Molina, L. T., Nenes, A., Oltmans, S. J., Parrish, D. D., Pederson, J. R., Pierce, R. B., Prather, K., Quinn, P. K., Seinfeld, J. H., Senff, C. J., Sorooshian, A., Stutz, J., Surratt, J. D., Trainer, M., Volkamer, R., Williams, E. J., and Wofsy, S. C.: The 2010 California Research at the Nexus of Air Quality and Climate Change (CalNex) field study, J. Geophys. Res., 118, 5830-5866, doi:10.1002/jgrd.50331, 2013.

Sarwar, G., Luecken, D., Yarwood, G., Whitten, G., and Carter, W. P. L.: Impact of an updated carbon bond mechanism on predictions from the Community Multiscale Air Quality Model, J. Appl. Meteorol. Climatol., 47, 3-14, doi:10.1175/2007JAMC1393.1, 2008.

1240 Seethala, C. and Horvath, Á.: Global assessment of AMSR-E and MODIS cloud liquid
1241 water path retrievals in warm oceanic clouds, J. Geophys. Res., 115, D13202,
1242 doi:10.1029/2009JD012662, 2010.

1243 Shrivastava, M. K., Lane, T. E., Donahue, N. M., Pandis, S. N., and Robinson, A. L.:
1244 Effects of gas particle partitioning and aging of primary emissions on urban and
1245 regional organic aerosol concentrations, J. Geophys. Res., 113, D18301,
1246 doi:10.1029/2007JD009735, 2008.

1247 Shrivastava, M., Easter, R., Liu, X., Zelenyuk, A., Singh, B., Zhang, K., Ma, P-L, Chand,
1248 D., Ghan, S., Jimenez, J.L., Zhang, Q., Fast, J., Rasch, P. and Tiitta, P.: Global
1249 transformation and fate of SOA: Implications of low volatility SOA and gas-phase
1250 fragmentation reactions, J. Geophys. Res. Atmos., 120, 4169-4195,
1251 doi:10.1002/2014JD022563, 2015.

1252 Shrivastava, M., Zelenyuk, A., Imre, D., Easter, R., Beranek, J., Zaveri, R. A., and Fast,
1253 J.: Implications of low volatility SOA and gas-phase fragmentation reactions on SOA
1254 loadings and their spatial and temporal evolution in the atmosphere, J. Geophys.
1255 Res., 118, 3328-3342, doi:10.1029/jgrd.50160, 2013.

1256 Smith S. J., van Aardenne, J., Klimont, Z., Andres, R., Volke, A., Delgado Arias, S.:
1257 Anthropogenic sulfur dioxide emissions: 1850-2005. Atmos Chem Phys., 11, 1101-
1258 1116. doi:10.5194/acp-11-1101-2011, 2011.

1259 Stainer, C. O., Donahue, N., and Pandis, S. N.: Parameterization of secondary organic
1260 aerosol mass fractions from smog chamber data, Atmos. Environ., 42, 2276-2299,
1261 doi:10.1016/j.atmosenv.2007.12.042, 2008.

1262 Taylor, K. E: Summarizing multiple aspects of model performance in a single diagram, J.
1263 Geophys. Res., 106, 7183-7192, 2001.

1264 Tilmes, S., Lamarque, J.-F., Emmons, L. K., Kinnison, D. E., Ma, P.-L., Liu, X., Ghan, S.,
1265 Bardeen, C., Arnold, S., Deeter, M., Vitt, F., Ryerson, T., Elkins, J. W., Moore, F.,
1266 Spackman, R., and Martin, M. V.: Description and evaluation of tropospheric
1267 chemistry and aerosols in the Community Earth System Model (CESM1.2), Geosci.
1268 Model Dev., 8, 1395-1426, doi:10.5194/gmd-8-1395-2015, 2015.

1269 Tsimpidi, A. P., Karydis, V. A., Zavala, M., Lei, W., Molina, L., Ulbrich, I. M., Jimenez,
1270 J. L., and Pandis, S. N.: Evaluation of the volatility basis-set approach for the
1271 simulation of organic aerosol formation in the Mexico City metropolitan area,
1272 Atmos. Chem. Phys., 10, 525-546, doi:10.5194/acp-10-525-2010, 2010.

1273 Vehkamaki, H., Kulmala, M., Napari, I., Lehtinen, K. E. J., Timmreck., C., Noppel, M.,
1274 and Laaksonen, A.: an improved parameterization for sulfuric acid-water nucleation
1275 rates for tropospheric and stratospheric conditions, Journal of Geophysical Research-
1276 Atmospheres, 107(D22), 4622, doi:10.1029/2002JD002184, 2002.

1277 Wang, M. and Penner, J. E.: Aerosol indirect forcing in a global model with particle
1278 nucleation, Atmos. Chem. Phys., 9, 239-260, 2009.

1279 Wang, K., Yahya, K., Zhang, Y., Wu, S.-Y., and Grell G.: Implementation and initial
1280 application of a new chemistry-aerosol option in WRF/Chem for simulation of
1281 secondary organic aerosols and aerosol indirect effects, Atmos. Environ, 115,
1282 doi:10.1016/j.atmosenv.2014.12.007, 2014.

1283 Wang, H., Easter, R. C., Rasch, P. J.,Wang, M., Liu, X., Ghan, S. J., Qian, Y., Yoon, J.-H.,
1284 Ma, P.-L., and Vinoj, V.: Sensitivity of remote aerosol distributions to representation
1285 of cloud–aerosol interactions in a global climate model, Geosci. Model Dev., 6, 765-
1286 782, doi:10.5194/gmd-6-765-2013, 2013.

1287 Washenfelder, R., Young, C., Brown, S., Angevine, W., Atlas, E., Blake, D., Bon, D.,
1288 Cubison, M., De Gouw, J., Dusanter, S., Flynn, J., Gilman, J. B., Graus, M., Griffith,
1289 S., Grossberg, N., Hayes, P. L., Jimenez, J., Kuster, W., Lefer, B. L., Pollack, I.,
1290 Ryerson, T., Stark, H., Stevens, P. S., and Trainer, M.: The glyoxal budget and its
1291 contribution to organic aerosol for Los Angeles, California, during CalNex 2010, J.
1292 Geophys. Res., 116, D00V02, doi:10.1029/2011JD016314, 2011.

1293 Young, P. J., Archibald, A. T., Bowman, K. W., Lamarque, J.-F., Naik, V., Stevenson, D.
1294 S., Tilmes, S., Voulgarakis, A., Wild, O., Bergmann, D., Cameron-Smith, P., Cionni,
1295 I., Collins, W. J., Dalsøren, S. B., Doherty, R. M., Eyring, V., Faluvegi, G., Horowitz,
1296 L. W., Josse, B., Lee, Y. H., MacKenzie, I. A., Nagashima, T., Plummer, D. A., Righi,
1297 M., Rumbold, S. T., Skeie, R. B., Shindell, D. T., Strode, S. A., Sudo, K., Szopa, S.,
1298 and Zeng, G.: Pre-industrial to end 21st century projections of tropospheric ozone
1299 from the Atmospheric Chemistry and Climate Model Intercomparison Project
1300 (ACCMIP), Atmos. Chem. Phys., 13, 2063-2090, doi:10.5194/acp-13-2063-2013,
1301 2013.

1302 Yarwood, G., Kemball-Cook, S., Johnson, J, Wilson, G, Dornblaser, B, and Estes, M:
1303 Evaluating NOx Emission Inventories for Air Quality Modeling Using Satellite,
1304 Model and SEARCH NO_2 Data, 11th Annual CMAS Conference, Chapel Hill, NC,
1305 October 16, 2012.

1306 Yarwood, G., Rao, S., Yocke, M., and Whitten, G. Z.: Updates to the carbon bond
1307 mechanism: CB05, Report to the U.S. Environmental Protection Agency, RT-04-

1308 00675, 2005.

1309 Yu, F.: Ion-mediated nucleation in the atmosphere: Key controlling parameters,
1310 implications, and look-up table, J. Geophys. Res., 115, D03206, doi:
1311 10.1029/2009JD012630, 2010.

1312 Yu, S.-C., Mathur, R., Sarwar, G., Kang, D., Tong, D., Pouliot, G., and Pleim, J.: Eta-
1313 CMAQ air quality forecasts for O_3 and related species using three different
1314 photochemical mechanisms (CB4, CB05, SAPRC-99): comparisons with
1315 measurements during the 2004 ICARTT study, Atmos. Chem. Phys., 10, 3001-3025,
1316 2010.

1317 Yu, S.-C., Dennis, R., Roselle, S., Nenes, A., Walker, J., Eder, B., Schere, K., Swall, J.,
1318 Robarge, W.: An assessment of the ability of 3-D air quality models with current
1319 thermodynamic equilibrium models to predict aerosol NO_3^-, J. Geophys. Res., 110,
1320 D07S13, doi:10.1029/2004JD004718, 2005.

1321 Yu, S.-C., Eder, B., Dennis, R., Chu, S.-H., Schwartz, S.: New unbiased symmetric
1322 metrics for evaluation of air quality models, Atmos. Sci. Let., 7, 26-34, 2006.Zender,
1323 C. S., Bian, H., and Newman, D.: The mineral Dust Entrainment And Deposition
1324 (DEAD) model: Description and 1990s dust climatology, J. Geophys. Res.,
1325 108(D14), 4416, doi: 10.1029/2002JD002775, 2003.

1326 Zhang, Q., Jimenez, J. L., Canagaratna, M. R., Allan, J. D., Coe, H., Ulbrich, I., Alfarra,
1327 M. R., Takami, A., Middlebrook, A. M., Sun, Y. L., Dzepina, K., Dunlea, E.,
1328 Docherty, K., DeCarlo, P. F., Salcedo, D., Onasch, T., Jayne, J. T., Miyoshi, T.,
1329 Shimono, A., Hatakeyama, S., Takegawa, N., Kondo, Y., Schneider, J., Drewnick,
1330 F., Borrmann, S., Weimer, S., Demerjian, K., Williams, P., Bower, K., Bahreini, R.,
1331 Cottrell, L., Griffin, R. J., Rautiainen, J., Sun, J. Y., Zhang, Y. M., and Worsnop, D.
1332 R.: Ubiquity and dominance of oxygenated species in organic aerosols in
1333 anthropogenically-influenced Northern Hemisphere midlatitudes, Geophys. Res.
1334 Lett., 34, L13801, doi:10.1029/2007GL029979, 2007.

1335 Zhang, Q., Quan, J., Tie, X., Huang, M., and Ma, X.: Impacts of aerosol particles on
1336 cloud formation: Aircraft measurements in China, Atmospheric Environment, 45,
1337 665-672, 2011.

1338 Zhang, Y., Liu, P., Pun, B., and Seigneur, C.: A comprehensive performance evaluation
1339 of MM5-CMAQ for summer 1999 Southern Oxidants Study episode, Part I.
1340 Evaluation protocols, databases, and meteorological predictions, Atmos. Environ.,
1341 40, 4825-4838, 2006.

Zhang, Y., Pun, B., Vijayaraghavan, K., Wu, S.-Y., Seigneur, C., Pandis, S., Jacobson, M., Nenes A., and Seinfeld, J. H.: Development and Application of the Model of Aerosol Dynamics, Reaction, Ionization and Dissolution (MADRID), Journal of Geophysical Research, 109, D01202, doi:10.1029/2003JD003501, 2004.

Zhang, Y., Karamchandani, P., Glotfelty, T., Street, D. G., Grell, G., Nenes, A., Yu, F., and Bennartz, R.: Development and initial application of the global-through-urban weather research and forecasting model with chemistry (GU-WRF/Chem), J. Geophys. Res., 117, D20206, doi:10.1029/2012JD017966, 2012a.

Zhang, Y., Chen, Y., Sarwar, G., and Schere, K.: Impacts of gas-phase mechanisms on weather research forecasting model with chemistry (WRF/Chem) predictions: Mechanism implementation and comparative evaluation, J. Geophys. Res., 117, D01301, doi: 10.1029/2011JD015775, 2012b.

Zhang, Y., Zhang, X., Wang, L.-T., Zhang, Q., Duan, F.-K., and He, K.-B.: Application of WRF/Chem over East Asia: Part I. Model Evaluation and Intercomparison with MM5/CMAQ, Atmospheric Environment, in press, doi:10.1016/j.atmosenv.2015.07.022, 2015a.

Zhang, Y., Zhang, X., Wang, K., Zhang, Q., Duan, F.-K., and He, K.-B.: Application of WRF/Chem over East Asia: Part II. Model Improvement and Sensitivity Simulations, Atmospheric Environment, in press, doi:10.1016/j.atmosenv.2015.07.023, 2015b.

Table 1. Gas-phase organic aerosol precursors in the two mechanisms

Precursors	MOZART-4x[1]	CB05_GE[2]
Aromatics	TOLUENE, BENZENE , XYLENES, CRESOL	TOL, XYL, CRES, PAH
Alkanes	BIGALK	ALKH
Anthropogenic alkenes	C3H6, BIGENE	OLE, IOLE
Biogenic alkenes	APIN, BPIN, LIMON, MYRC, BCARY, ISOP	APIN, BPIN, LIM, OCI, HUM, TER, ISOP

[1] BIGALK: lumped alkanes C > 3; C_3H_6: propene; BIGENE: lumped alkenes C > 3; APIN: α-pinene + others; BPIN: β-pinene+others; LIMON: limonene + others; MYRC: myrcene + others; BCARY: beta-caryophyllene + other sesquiterpenes; ISOP: isoprene.

[2] TOL: toluene and other monoalkyl aromatics; XYL: xylene and other polyalkyl aromatics; CRES: cresol and higher molecular weight phenols; PAH: polycyclic aromatic hydrocarbons; ALKH: long-chain alkanes, C >6; OLE: terminal olefin carbon bond (R-C=C); IOLE: internal olefin carbon bond (R-C=C-R); APIN: α-pinene; BPIN: β-pinene; LIM: limonene; OCI: ocimene; HUM: humulene; TER: terpinene; ISOP: isoprene.

Table 2. Datasets for model evaluation

Species/Variables	Dataset (Number of sites)
Cloud fraction (CF) Cloud optical thickness (COT) Cloud liquid water path (LWP) Precipitating water vapor (PWV) Aerosol optical depth (AOD) Column cloud condensation nuclei (ocean) at S = 0.5% (CCN5)	MODIS
Cloud droplet number concentration (CDNC), LWP	Bennartz (2007)
Shortwave cloud radiative forcing (SWCF) Longwave cloud radiative forcing (LWCF) Downwelling longwave radiation at surface (FLDS) Downwelling shortwave radiation at surface (FSDS)	CERES-EBAF
Outgoing longwave radiation (OLR)	NOAA/CDC
Carbon monoxide (CO)	East Asia: NIESJ (2133), TAQMN (70), KMOE (258)
Ozone (O_3)	CONUS: CASTNET (141) Europe: Airbase (3846), BDQA (490), EMEP (317) East Asia: TAQMN (70), KMOE (258)
Sulfur dioxide (SO_2)	CONUS: CASTNET (141) Europe: Airbase (3846), BDQA (490), EMEP (317) East Asia: MEPC (84), NIESJ (2133), KMOE (258), TAQMN (70)
Nitric acid (HNO_3)	CONUS: CASTNET (141); Europe: EMEP (317)
Ammonia (NH_3)	Europe: Airbase (3846), EMEP (317)
Nitrogen dioxide (NO_2)	CONUS: ARS (25877) Europe: Airbase (3846), BDQA (490), EMEP (317) East Asia: NIESJ, TAQMN, KMOE
Sulfate (SO_4^{2-}), Ammonium (NH_4^+), Nitrate (NO_3^-)	CONUS: CASTNET (141), IMPROVE (199), STN (18129); Europe: Airbase (3846), EMEP (317)
Chloride (Cl^-)	CONUS: IMPROVE (199) Europe: Airbase (3846), EMEP (317)
Organic carbon (OC)	CONUS: IMPROVE (199); Europe: EMEP (317)
Black carbon (BC), Total carbon (TC)	CONUS: IMPROVE (199), STN(18129)
Formaldehyde (HCHO), Isoprene (ISOP), and Toluene (TOL)	CONUS: AQS (25877)
Hydrocarbon-like organic aerosol (HOA), Oxygenated organic aerosol (OOA), Total organic aerosol (TOA)	Northern Hemisphere: Zhang et al. (2007) and Jimenez et al. (2009) (Z07 & J09) (33)
Secondary organic aerosol (SOA)	CONUS: Ohio (2) and California (2) (Lewandowski et al., 2013)
Particulate matter with diameter less than and equal to 2.5 μm ($PM_{2.5}$)	CONUS: IMPROVE (199), STN (18129) Europe: BDQA (490), EMEP (317)
Particulate matter with diameter less than and equal to 10 μm (PM_{10})	CONUS: AQS (25877) Europe: Airbase (3846), BDQA (490), EMEP (317) East Asia: MEPC (84), NIESJ (2133), KMOE (258), TAQMN (70)
Column CO	Globe: MOPITT
Column NO_2, Column SO_2, Column HCHO, Column glyoxal ($C_2H_2O_2$)	Globe: SCIAMACHY
Tropospheric ozone residual (TOR)	Globe: OMI/MLS
O_3, CO, NO_x, and NO_y profiles	ARCPAC (Mar.-Apr., 2008), ARCTAS (Apr.-Jun., 2008), START08 (Apr.-Jun., 2008), and CalNex (May-Jun., 2010)
CCN_China	Beijing: Zhang et al. (2011) (Jul.-Sep., 2008)

NOAA/CDC: National Oceanic and Atmospheric Administration Climate Diagnostics Center; MODIS: Moderate Resolution Imaging Spectroradiometer; CERES-EBAF: Clouds and Earth's Radiant Energy System-Energy Balanced and Filled product; MOPITT: the Measurements Of Pollution In The Troposphere; OMI/MLS: the Aura Ozone Monitoring Instrument in combination with Aura Microwave Limb Sounder; SCIAMCHY: the SCanning Imaging Absorption spectroMeter for Atmospheric CHartographY; CASTNET: Clean Air Status and Trends Network; IMPROVE: Interagency Monitoring of Protected Visual Environments; STN: Speciation Trends Network; AQS: Air Quality System; EMEP: European Monitoring and Evaluation Program; BDQA: Base de Données sur la Qualité de l'Air; AirBase: European air quality database; MEPC: Ministry of Environmental Protection of China; TAQMN: Taiwan Air Quality Monitoring Network; NIESJ: National Institute for Environmental Studies of Japan; KMOE: Korean Ministry of Environment; ARCPAC: Aerosol, Radiation, and Cloud Processes affecting Arctic Climate in 2008 (Brock et al., 2011); ARCTAS: Arctic Research of the Composition of the Troposphere from Aircraft and Satellites (Jacob et al., 2010), START08: Stratosphere-Troposphere Analyses of Regional Transport in 2008 (Pan et al., 2010); CalNex: California Nexus 2010 (Ryerson et al., 2013)..

Table 3. Performance statistics of chemical species

Species	Domain	Obs	MOZART-4x			CB05_GE		
			Sim	NMB (%)[6]	NME (%)[6]	Sim	NMB (%)[6]	NME (%)[6]
CO (ppb)	East Asia	438.7	150.9	-65.6	65.7	150.4	-65.7	65.8
SO_2[1]	CONUS	1.7	11.6	580.2	580.2	11.2	561.6	561.6
	Europe	4.7	9.5	100.9	121.2	9.2	94.1	115.4
	East Asia	2.9	4.3	47.0	70.6	3.9	35.5	64.0
NH_3 ($\mu g\ m^{-3}$)	Europe	1.2	2.5	112.4	146.0	2.4	104.3	139.8
NO_2[2]	CONUS	8.3	4.0	-51.4	55.9	4.0	-52.2	56.4
	Europe	17.4	6.7	-61.4	65.5	6.6	-62.1	66.0
	East Asia	11.7	3.0	-74.1	75.2	3.0	-74.8	75.8
O_3[3]	CONUS	34.7	44.7	29.0	29.5	44.4	28.2	28.5
	Europe	56.2	78.6	39.9	40.8	80.6	43.5	44.2
	East Asia	29.8	48.3	62.4	62.4	47.7	60.3	60.3
HNO_3 ($\mu g\ m^{-3}$)	CONUS	0.9	2.1	145.0	145.2	2.2	154.7	154.7
	Europe	0.8	0.7	-15.6	65.4	0.8	-10.9	64.9
HCHO (ppb)	CONUS	2.3	1.6	-30.1	48.4	1.5	-36.3	49.0
ISOP (ppb)	CONUS	0.3	0.2	-27.3	63.2	0.2	-29.0	64.7
Toluene (ppb)	CONUS	0.5	0.2	-65.3	69.2	0.2	-65.1	69.1
Col. CO ($molec.cm^{-2}$)	Globe	1.6×10^{18}	1.2×10^{18}	-25.8	27.5	1.2×10^{18}	-24.4	26.1
Col. NO_2 ($molec.cm^{-2}$)	Globe	5.5×10^{14}	8.5×10^{14}	56.0	71.0	9.3×10^{14}	70.2	83.3
Col. HCHO ($molec.cm^{-2}$)	Globe	4.6×10^{15}	3.1×10^{15}	-31.2	39.2	3.1×10^{15}	-32.7	40.4
Col. C2H2O2 ($molec.cm^{-2}$)	Globe	2.8×10^{14}	3.9×10^{13}	-86.0	86.0	5.9×10^{12}	-97.9	-97.9
Col. SO_2(DU)	Globe	1.2	0.3	-70.1	90.1	0.3	-73.5	88.7
TOR (DU)	Globe	28.6	30.3	6.0	15.0	31.8	11.3	16.5
SO_4^{2-} ($\mu g\ m^{-3}$)	CONUS	1.8	3.0	72.9	72.9	3.3	89.7	89.7
	Europe	1.8	2.9	62.1	70.1	3.2	79.7	85.2
NH_4^+ ($\mu g\ m^{-3}$)	CONUS	0.9	1.3	37.8	49.9	1.3	44.3	55.6
	Europe	0.9	1.3	51.5	63.1	1.4	63.4	72.8
NO_3^- ($\mu g\ m^{-3}$)	CONUS	0.9	0.9	-6.0	44.4	0.7	-21.2	40.2
	Europe	1.7	1.2	-28.9	54.2	1.2	-30.5	53.4
Cl^- ($\mu g\ m^{-3}$)	CONUS	0.1	0.02	-78.1	84.3	0.02	-78.3	84.5
	Europe	1.1	4.1	273.4	274.7	4.2	273.7	274.8
BC ($\mu g\ m^{-3}$)	CONUS	0.3	0.2	-29.3	44.6	0.2	-29.3	44.6
OC ($\mu g\ m^{-3}$)	CONUS	0.9	1.0	2.1	33.2	0.7	-20.7	32.8
	Europe	2.9	0.7	-74.2	77.3	0.7	-75.1	78.0
TC ($\mu g\ m^{-3}$)	CONUS	1.8	1.3	-29.6	39.3	1.1	-42.1	45.8
SOA[4]	CONUS	1.8	1.8	-1.9	29.3	1.4	-23.1	35.8
HOA[4]	N.H.[5]	2.1	0.5	-77.2	81.5	0.5	-76.7	81.3
OOA[4]	N.H.[5]	4.8	2.1	-56.5	56.6	1.8	-62.3	62.3
TOA[4]	N.H.[5]	7.9	2.5	-67.8	68.2	2.3	-71.2	72.0
$PM_{2.5}$ ($\mu g\ m^{-3}$)	CONUS	7.4	10.3	38.9	58.1	10.3	37.7	58.6
	Europe	14.4	11.5	-20.4	48.4	11.8	-18.3	47.0
PM_{10} ($\mu g\ m^{-3}$)	CONUS	20.6	12.6	-38.6	50.2	12.6	-38.9	50.7
	Europe	22.1	18.8	-14.9	39.9	19.2	-13.1	38.9
	East Asia	88.0	59.0	-32.9	41.1	64.8	-26.4	37.2

[1] The unit is $\mu g\ m^{-3}$ for CONUS and ppb for East Asia. [2] The unit is $\mu g\ m^{-3}$ for Europe and ppb for CONUS and East Asia. [3] The unit is ppb for CONUS and East Asia, and $\mu g\ m^{-3}$ for Europe. [4] SOA: secondary organic aerosol; HOA: hydrocarbon-like organic aerosol; OOA: oxygenated organic aerosol; TOA: total organic aerosol; [5] N.H.: northern hemisphere; [6] MB: mean bias; NMB: normalized mean bias (%); NME: normalized mean error (%); RMSE: root mean squared error; Corr.: correlation coefficient.

Table 4. Performance statistics of cloud/radiative variables

Variables[1]	Networks	Obs	MOZART-4x					CB05_GE				
			Sim	NMB (%)[2]	NME (%)[2]	RMSE[2]	Corr[2]	Sim	NMB (%)[2]	NME (%)[2]	RMSE[2]	Corr[2]
OLR ($W\ m^{-2}$)	NOAA/ CDC	217.0	224.8	3.6	4.1	10.0	0.99	223.7	3.1	3.9	9.6	0.98
FLDS ($W\ m^{-2}$)	CERES	306.7	307.3	0.2	3.1	11.6	0.99	307.3	0.2	3.1	11.5	0.99
FSDS ($W\ m^{-2}$)	CERES	163.4	150.9	-7.6	10.2	22.6	0.9	150.8	-7.7	10.2	22.7	0.9
SWCF ($W\ m^{-2}$)	CERES	-40.7	-51.5	26.4	33.4	19.0	0.9	-52.0	27.7	-34.4	19.6	0.9
LWCF ($W\ m^{-2}$)	CERES	22.4	17.6	-21.6	25.1	6.8	0.9	18.7	-16.7	23.8	6.6	0.9
CCN5 ($\#\ cm^{-2}$)	MODIS	2.2×10^{8}	1.5×10^{8}	-32.1	46.4	1.7×10^{8}	0.4	1.6×10^{8}	-29.0	46.6	1.7×10^{8}	0.4
CF (%)	MODIS	67.3	71.5	6.3	12.7	12.5	0.8	71.3	6.0	12.7	12.5	0.8
COT	MODIS	16.5	12.2	-26.0	61.6	14.0	-0.3	12.2	-26.0	61.3	14.0	-0.3
AOD	MODIS	0.15	0.11	-23.9	40.5	0.08	0.7	0.11	-24.6	40.5	0.08	0.7
PWV (cm)	MODIS	1.9	2.0	5.6	11.4	0.3	0.99	2.0	5.5	11.4	0.3	0.99
CDNC ($\#\ cm^{-3}$)	Bennartz (2007)	105.8	126.6	19.7	38.7	56.5	0.5	127.8	20.8	39.1	58.1	0.6
LWP ($g\ m^{-2}$)	MODIS	142.0	65.2	-54.1	65.4	143.3	-0.4	64.7	-54.4	65.3	143.3	-0.4
	Bennartz (2007)	84.6	87.0	2.8	38.3	42.3	0.4	86.0	1.7	37.7	41.7	0.4

[1] OLR: outgoing long wave radiation; FLDS: downwelling longwave radiation at the surface; FSDS: downwelling shortwave radiation at the surface; SWCF: shortwave cloud radiative forcing; LWCF: longwave cloud radiative forcing; CCN5: column CCN (ocean) at supersaturation of 0.5%; CF: cloud fraction; COT: clout optical thickness; AOD: aerosol optical depth; PWV: precipitable water vapor; CDNC: cloud droplet number concentration; LWP: liquid water path.

[2] NMB: normalized mean bias (%); NME: normalized mean error (%); RMSE: root mean squared error; Corr.: correlation coefficient.

Table 5. Tropospheric Ozone Budget

Ozone	MOZART-4x	CB05_GE	Lamarque et al. (2012)	Young et al. (2013)
Burden (Tg)	325	333	328	337 ± 23
Dry Deposition (Tg yr^{-1})	679	705	705	1003 ± 200
[a] Chemical Production (Tg yr^{-1})	4974	5743	4897	5110 ± 606
[b] Chemical Loss (Tg yr^{-1})	4259	5194	4604	4668 ± 727
Lifetime (days)	24	21	26	22.3 ± 2.0

[a] Chemical production is mainly contributed by reactions of NO with peroxy radicals.

[b] Chemical loss is mainly contributed by the oxygen radical in the $O(^1D)$ + water (H_2O) reaction and by the reactions of ozone with the hydroperoxyl radical (HO_2), OH, and alkenes.

Figure captions

Figure 1. Scatter plots of O_3, PM, organic carbon (OC), secondary organic aerosol (SOA), hydrocarbon-like organic aerosol (HOA), oxygenated organic aerosol (OOA), total organic aerosol (TOA) over various sites during 2008-2010.

Figure 2. Comparisons of simulated and observed SOA concentrations at the four field study sites during 2009-2010. The observations are based on Lewandowski et al. (2013).

Figure 3. Zonal-mean profiles of HCHO, glyoxal, CO, NO_2, and TOR from CB05_GE and MOZART-4x simulations for June, July, and August during 2008-2010.

Figure 4. Simulated vertical profiles of O_3, CO, NO_x, and NO_y, against aircraft measurements. The black solid line represents observations from aircraft measurements (Pan et al., 2010; Brock et al., 2011; Ryerson et al., 2011; Jacob et al., 2010). The red solid and blue solid lines represent model output from MOZART-4x and CB05_GE, respectively.

Figure 5. Simulated vertical profiles of CCN against aircraft measurements. The black solid line represents observations from aircraft measurements of Zhang et al. (2011). The red solid and blue solid lines represent model output from MOZART-4x and CB05_GE, respectively.

Figure 6. Taylor diagram of comparison of cloud and radiative predictions between MOZART-4x and CB05_GE.

Figure 7. Comparison of satellite observations with predictions of AOD, CCN5, CDNC, COT, and SWCF by MOZART-4x and CB05_GE.

Figure 8a. Absolute differences averaged during 2008-2010 in tropospheric column concentrations of major gaseous species between MOZART-4x and CB05_GE.

Figure 8b. Absolute differences averaged during 2008-2010 in tropospheric column concentrations of major aerosol species between MOZART-4x and CB05_GE.

Figure 9. Column abundances (mg m^{-2}) averaged during 2008-2010 of secondary organic aerosols (SOA) from anthropogenic sources (ASOA), biogenic sources (BSOA), and glyoxal (GLSOA), and semi-volatile organic aerosol (SVSOA) over Australia, Europe, North America, South Africa, South America, and East Asia.

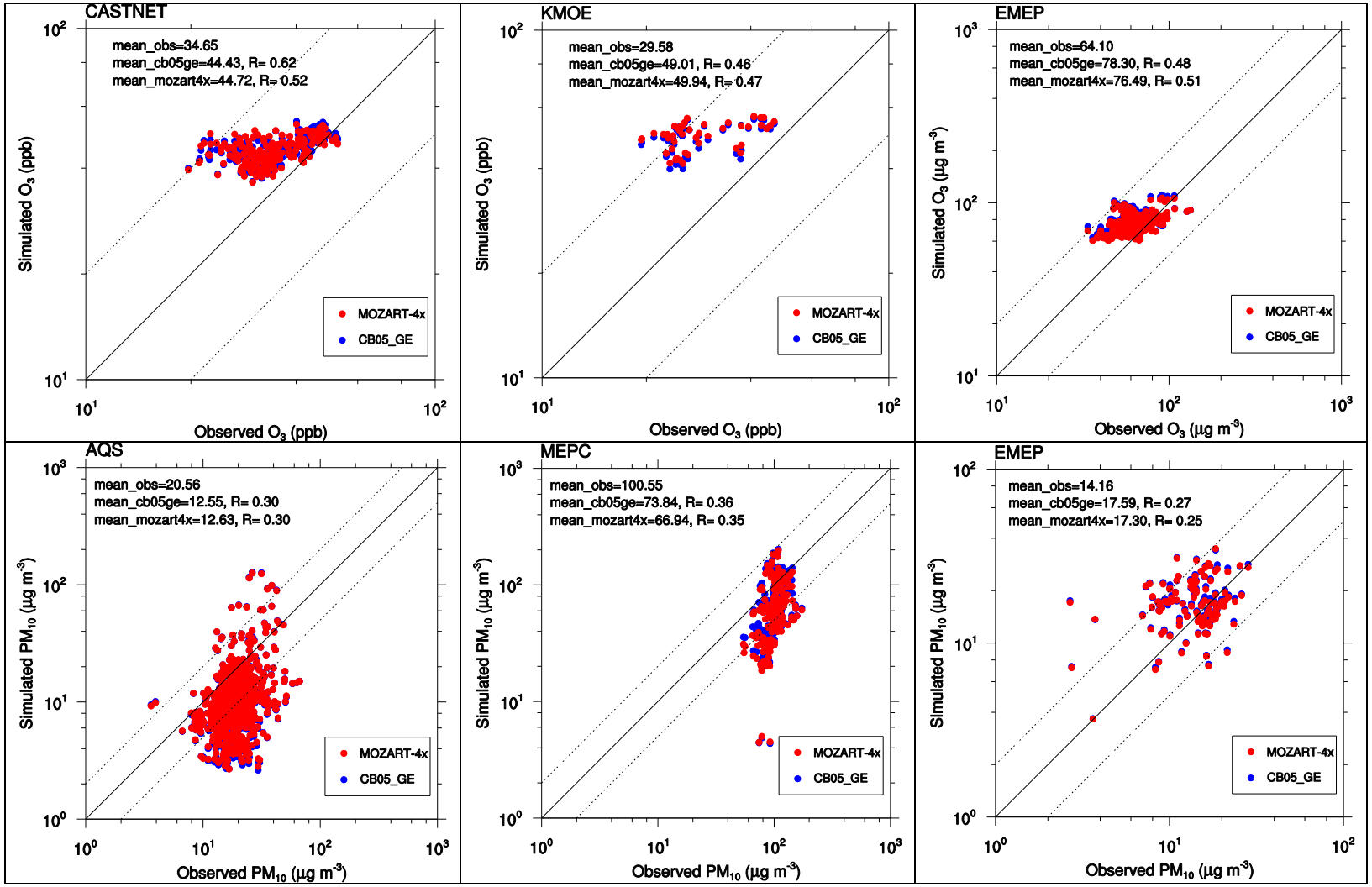

Figure 1. Scatter plots of O_3, PM, organic carbon (OC), secondary organic aerosol (SOA), hydrocarbon-like organic aerosol (HOA), oxygenated organic aerosol (OOA), total organic aerosol (TOA) from various sites during 2008-2010. The X (observations) and Y (simulations) axes are in log scale. Red dots represent MOZART-4x and blue dots represent CB05_GE. R is the correlation coefficient between simulated results and observational data. Z07: Zhang et al. (2007); J09: Jimenez et al. (2009); L13: Lewondowski et al. (2013).

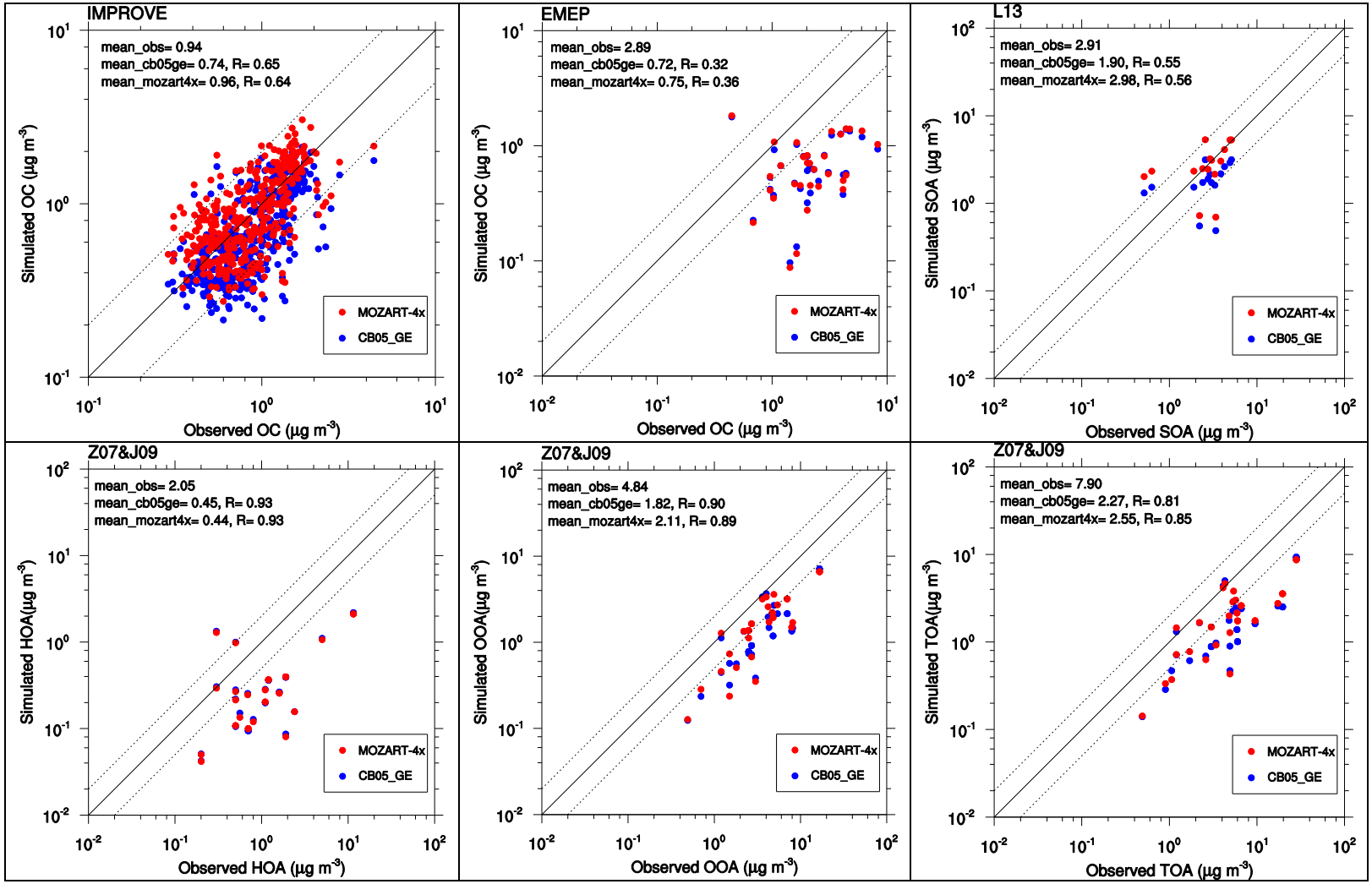

Figure 1. Continued.

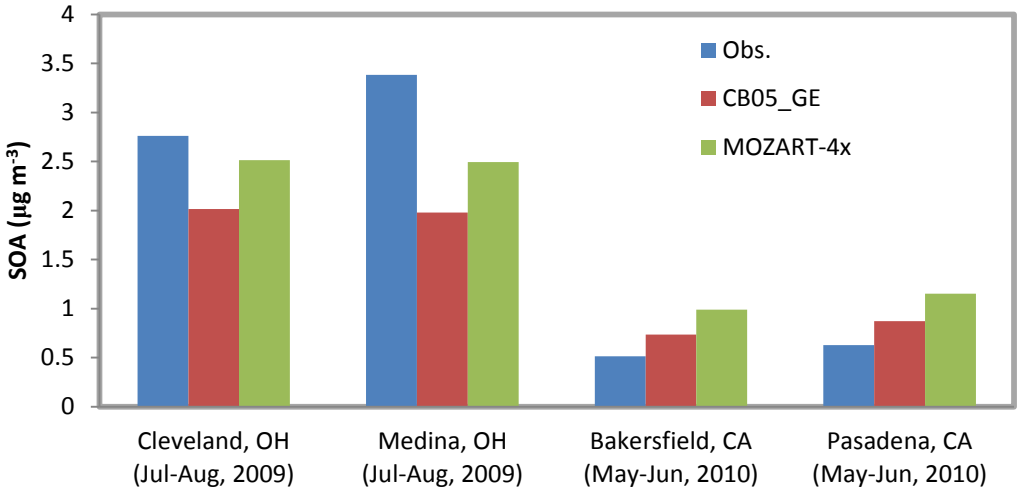

Figure 2. Comparisons of simulated and observed SOA concentrations at the four field study sites during 2009-2010. The observations are based on Lewandowski et al. (2013).

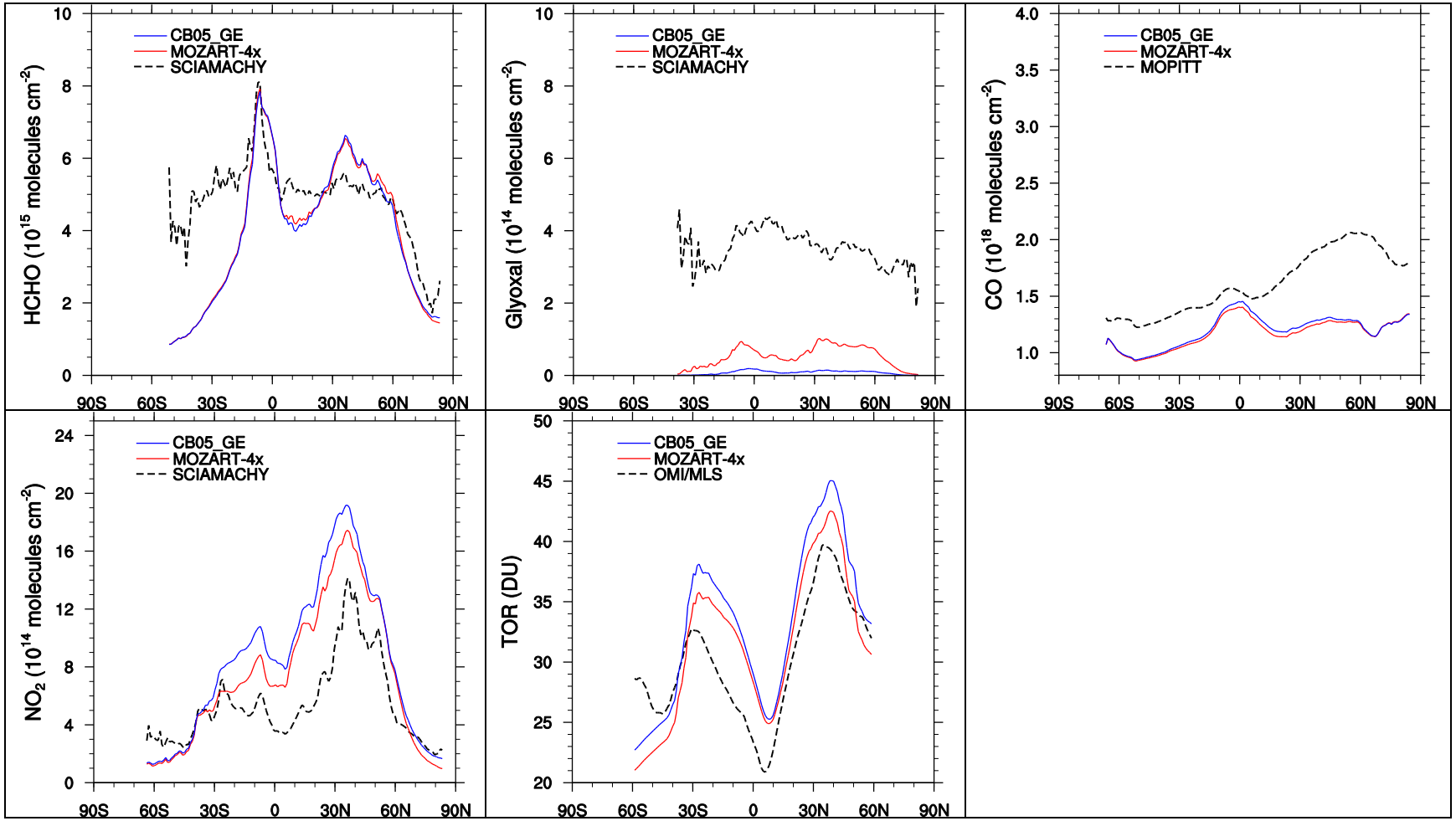

Figure 3. Zonal-mean profiles of HCHO, glyoxal, CO, NO_2, and TOR from CB05_GE and MOZART-4x simulations for June, July, and August during 2008-2010.

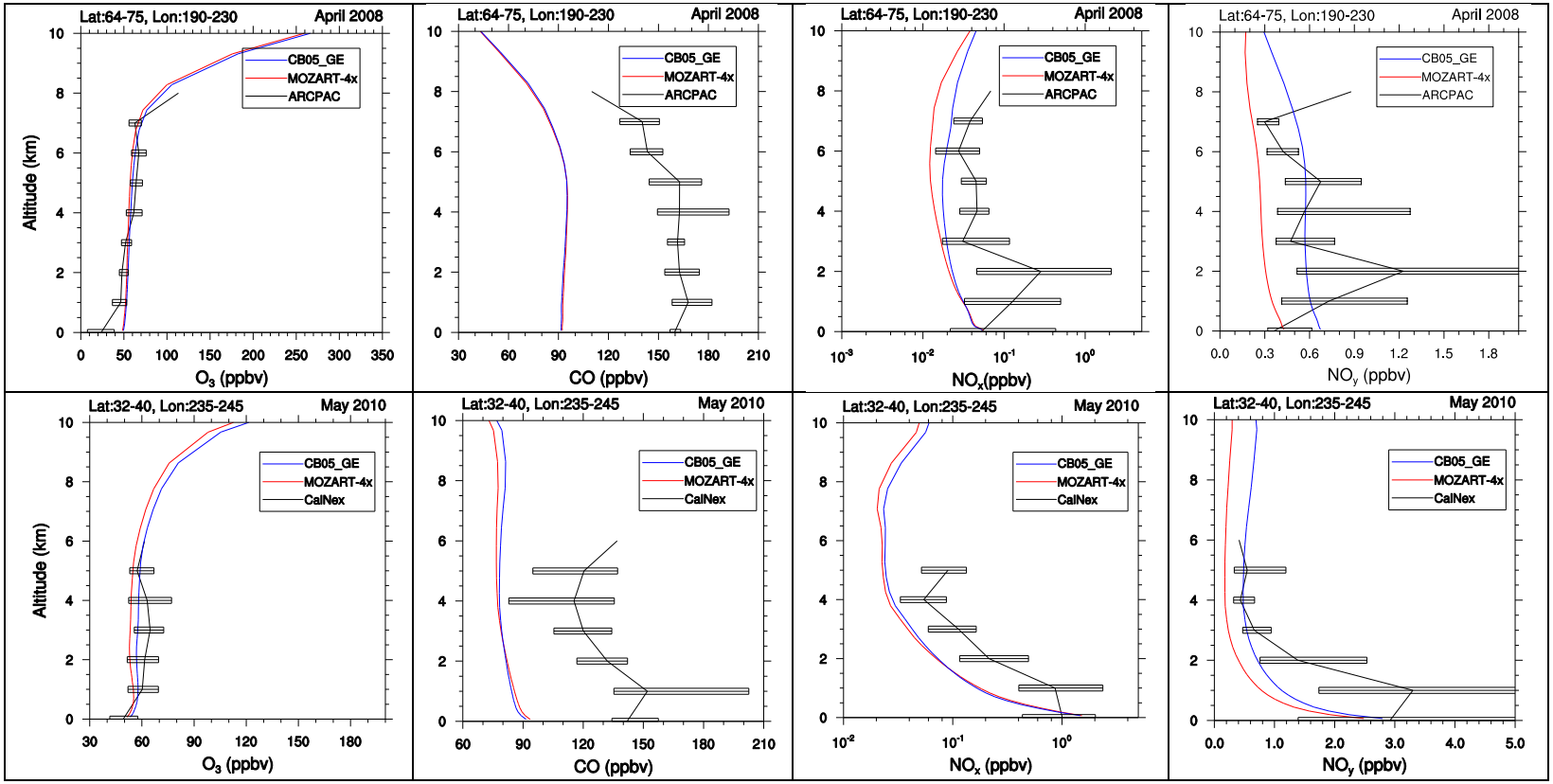

Figure 4. Simulated vertical profiles of O_3, CO, NO_x, NO_y (including aerosol nitrate), OH and H_2O_2, against aircraft measurements. The black solid line represents observations from aircraft measurements (Pan et al., 2010; Brock et al., 2011; Ryerson et al., 2011; Jacob et al., 2010; Zhang et al., 2011). The red solid and blue solid lines represent model output from MOZART-4x and CB05_GE, respectively.

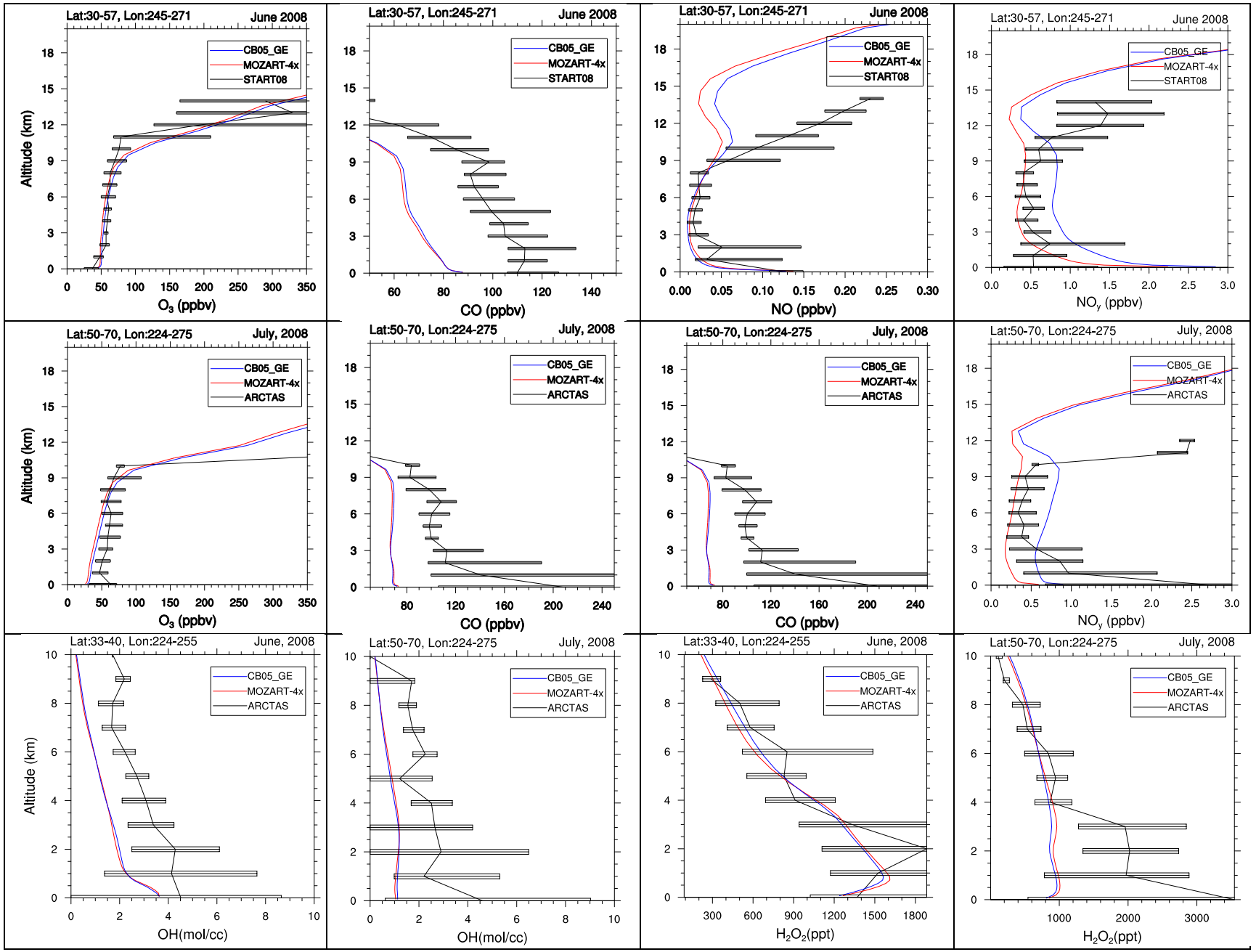

Figure 4. Continued.

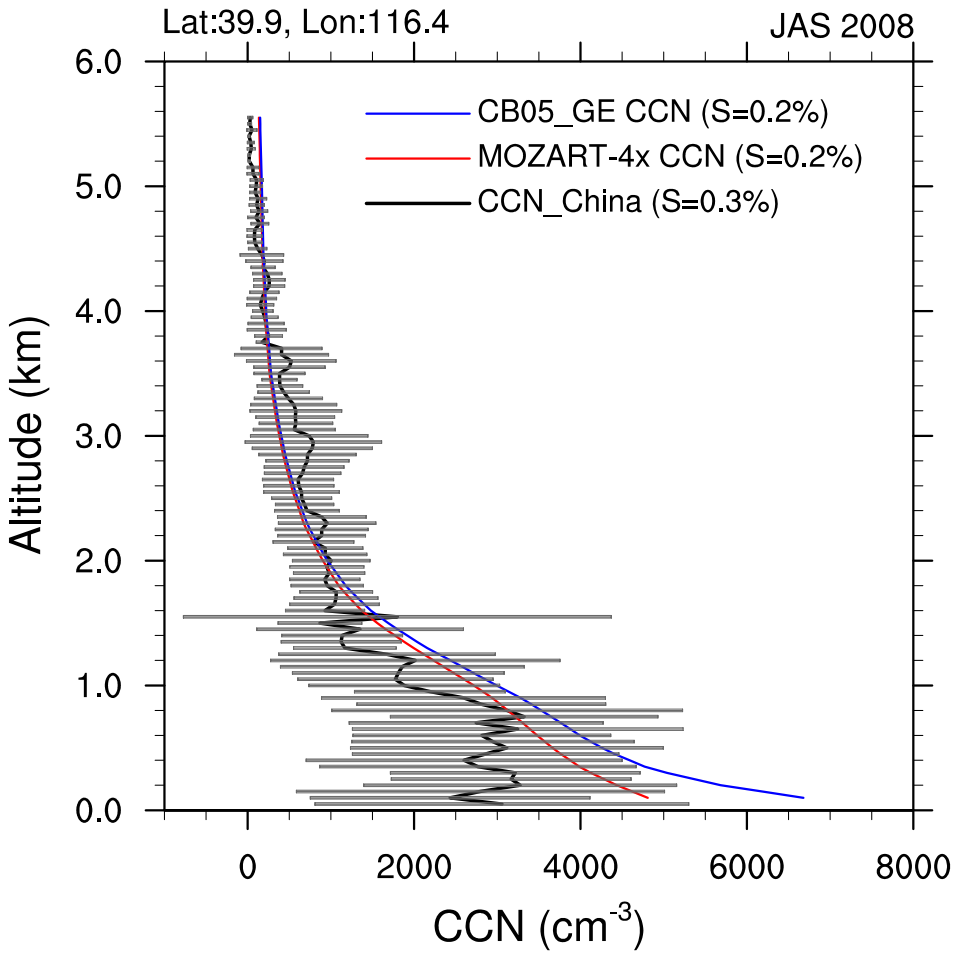

Figure 5. Simulated vertical profiles of CCN against aircraft measurements. The black solid line represents observations from aircraft measurements of Zhang et al. (2011). The red solid and blue solid lines represent model output from MOZART-4x and CB05_GE, respectively.

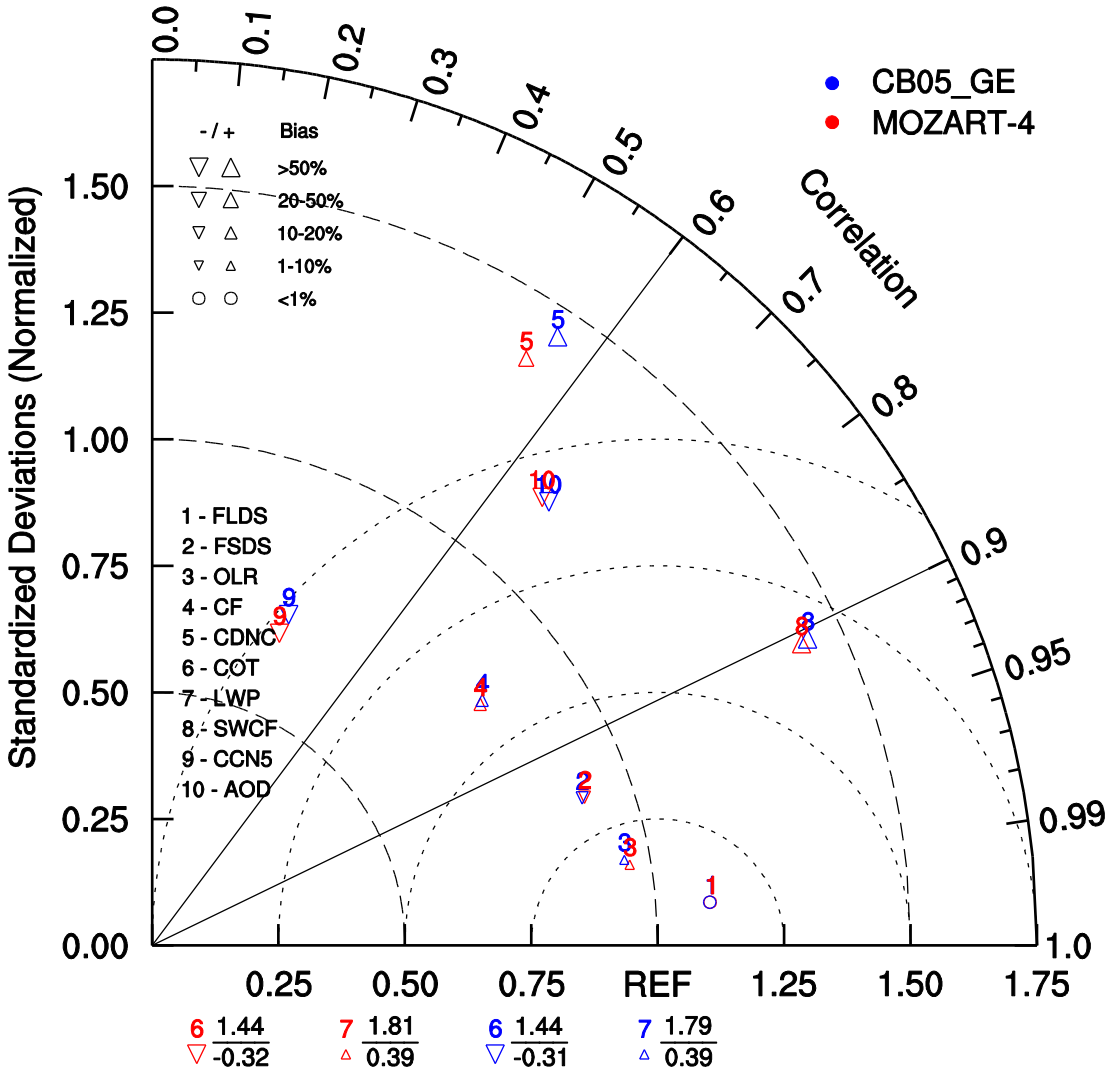

Figure 6. Taylor diagram of comparison of cloud and radiative predictions between MOZART-4x and CB05_GE. The results are based on 3-year average. This diagram represents the similarity between MOZART-4x and CB05_GE. X-axis represents the ratio of variances between observations and simulations (proportional to the reference point identified as "REF"), and Y-axis represents the normalized standard deviation between the two patterns (proportional to the radial distance from the origin). Two variables, COT and LWP, are located outside the diagram because the ratios of variance between simulated results and observations (the values of 1.81 from MOZART-4x and 1.79 from CB05_GE in the top) are larger than 1.75 for LWP and the correlation coefficients (the values of -0.32 from MOZART-4x and -0.31 from CB05_GE in the bottom) for COT are negative.

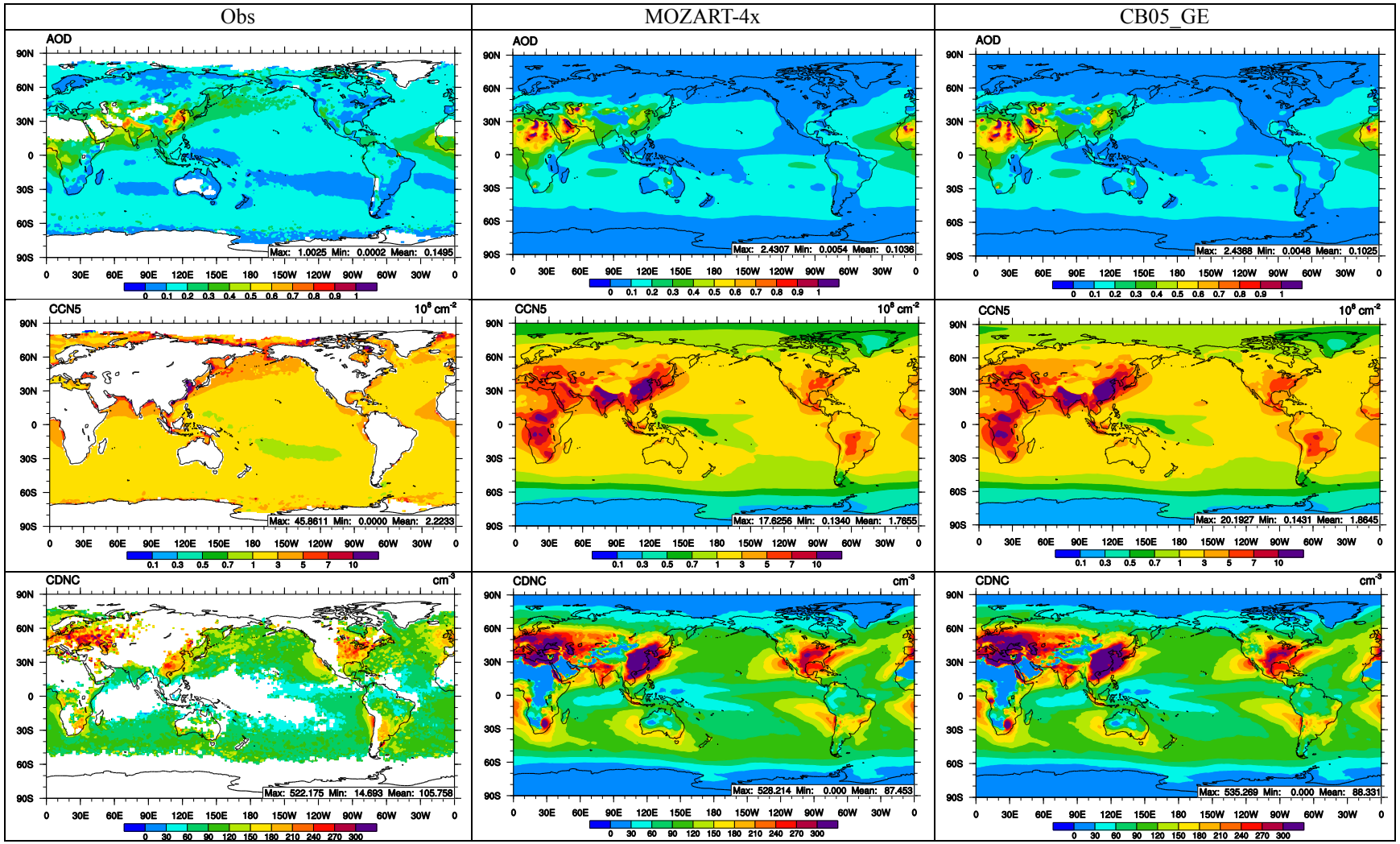

Figure 7. Comparison of satellite observations with predictions of for AOD, CCN5, CDNC, COT, and SWCF by MOZART-4x and CB05_GE.

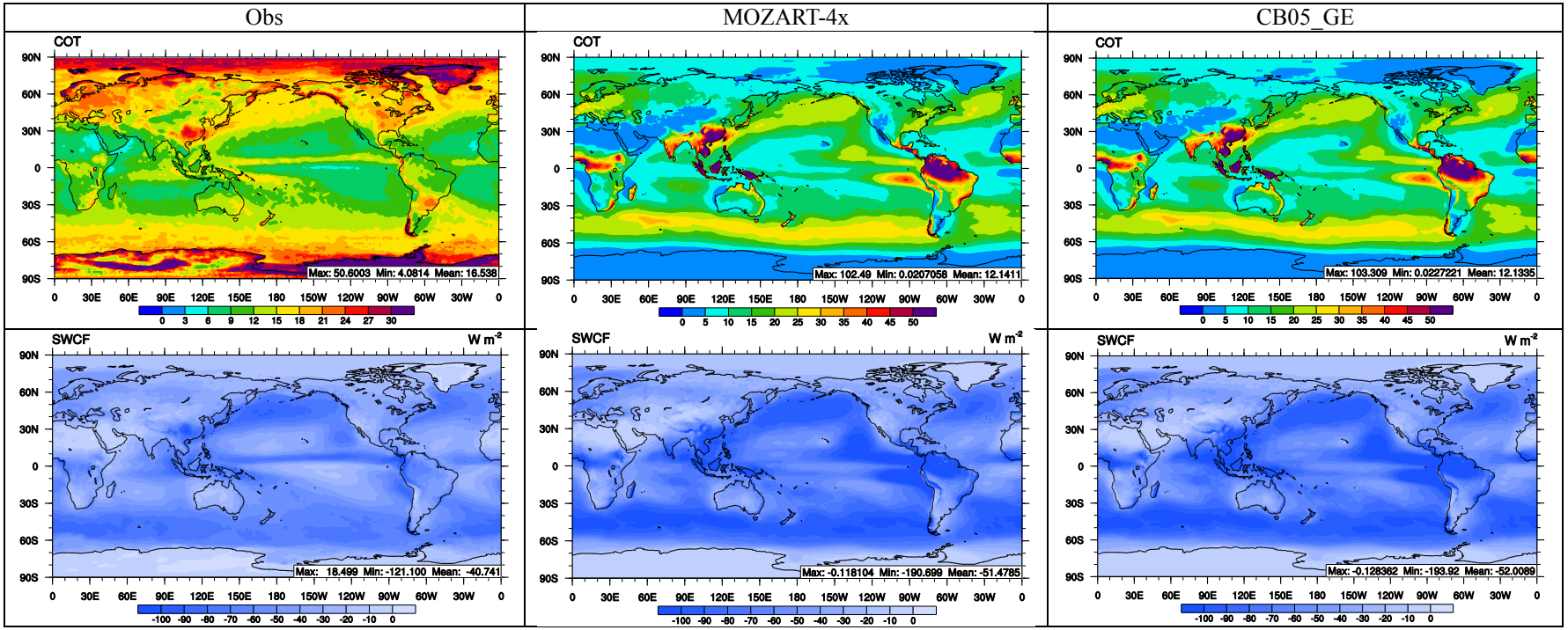

Figure 7. continued.

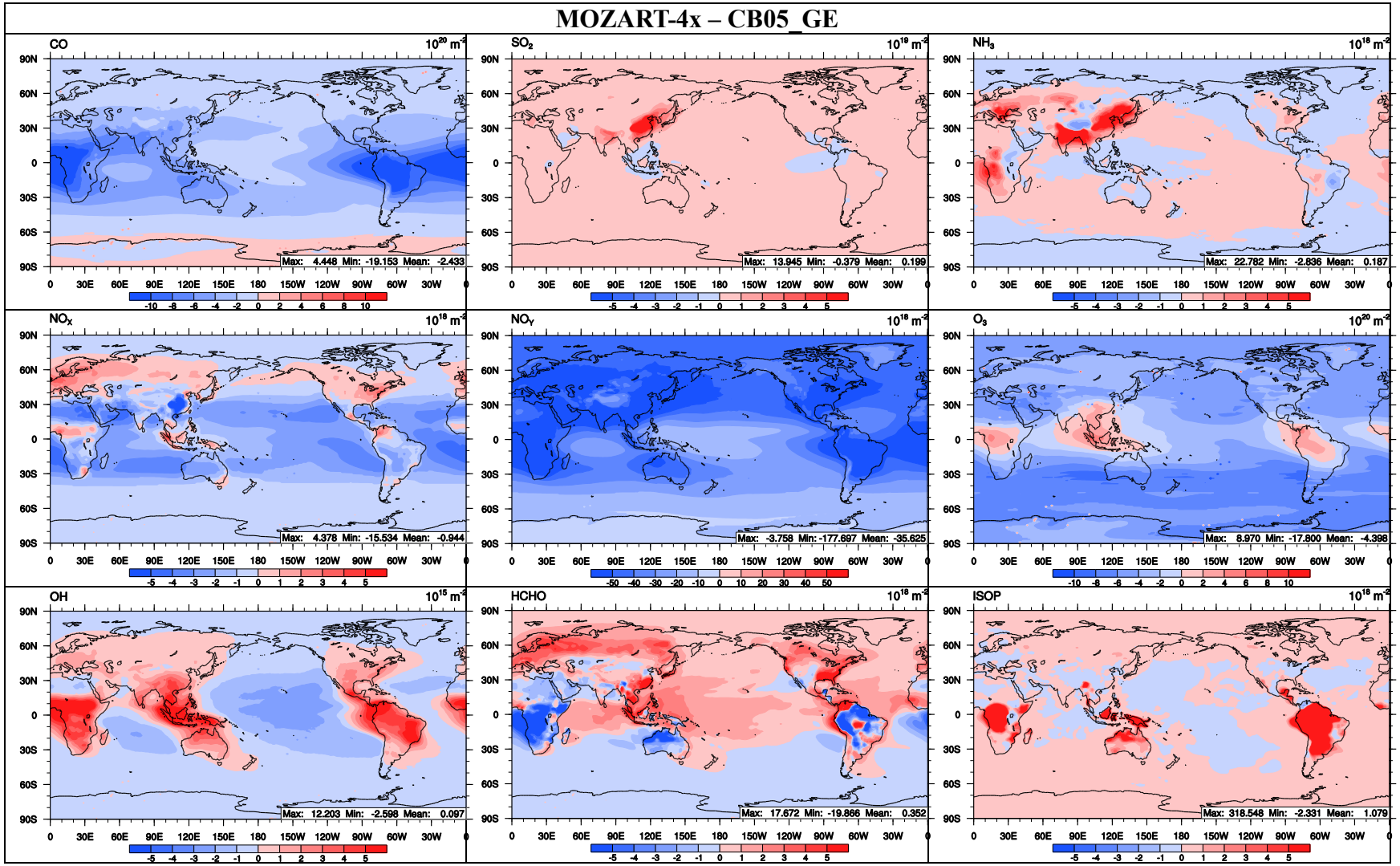

Figure 8a. Absolute differences averaged during 2008-2010 in tropospheric column concentrations of major gaseous species between MOZART-4x and CB05_GE.

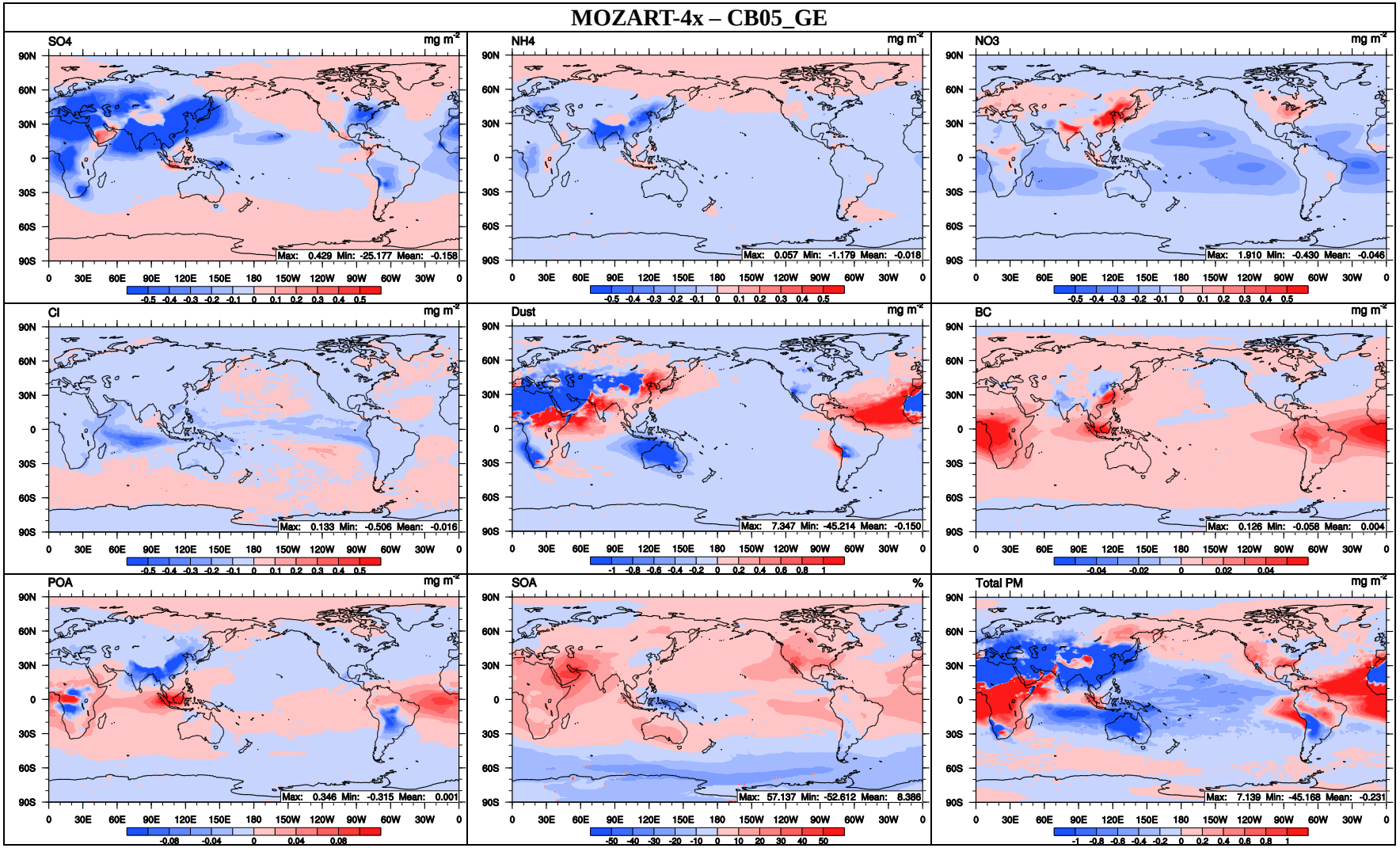

Figure 8b. Absolute differences averaged during 2008-2010 in tropospheric column concentrations of major aerosol species between MOZART-4x and CB05_GE.

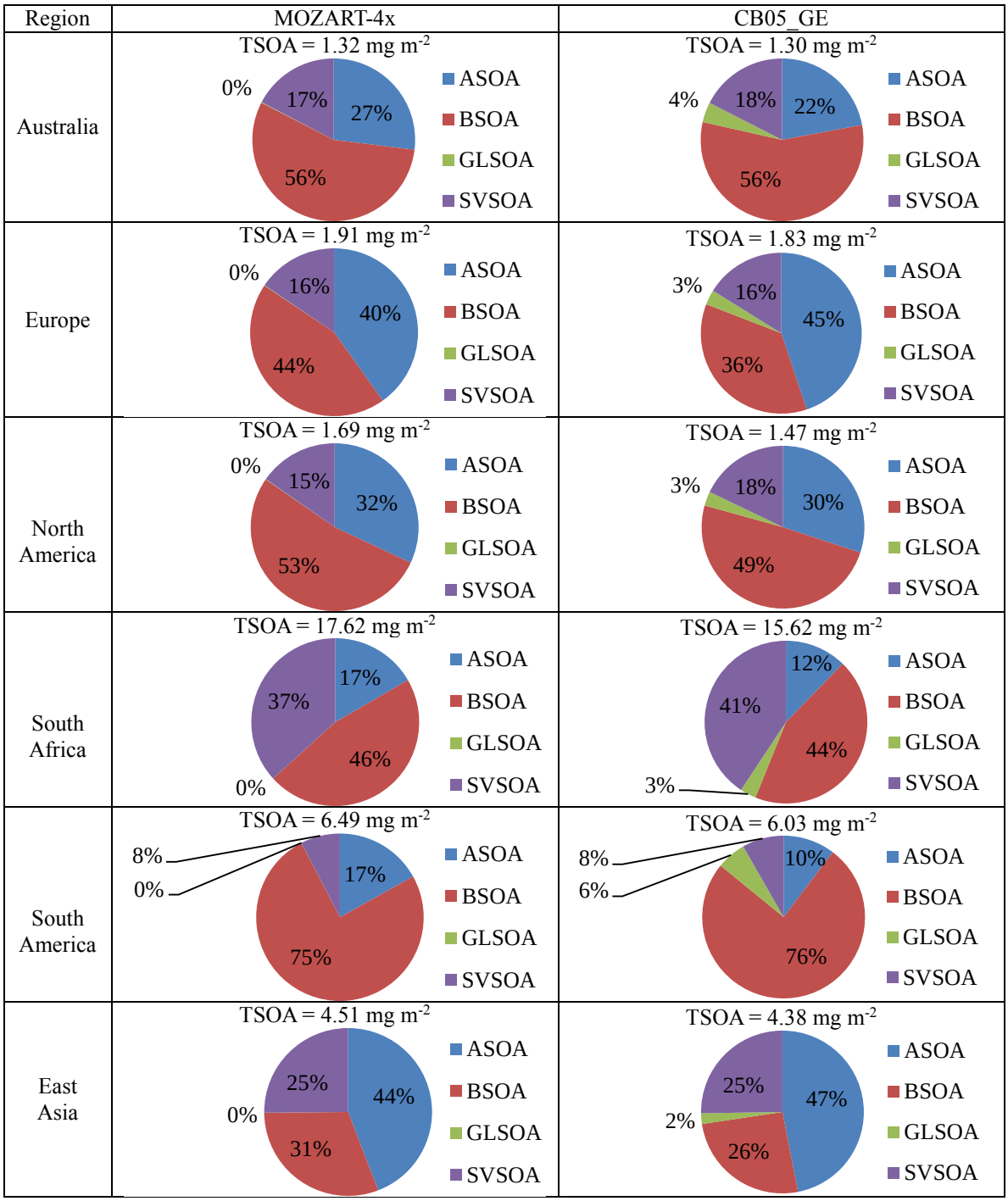

Figure 9. Column abundances (mg m^{-2}) averaged during 2008-2010 of secondary organic aerosols (SOA) from anthropogenic sources (ASOA), biogenic sources (BSOA), and glyoxal (GLSOA), and semi-volatile organic aerosol (SVSOA) over Australia, Europe, North America, South Africa, South America, and East Asia.